Emitted Power Of Jupiter Based On Cassini CIRS And VIMS Observations

Liming Li[1*], Kevin H. Baines[2], Mark A. Smith[1], Robert A. West[2], Santiago Perez-Hoyos[3], Harold J. Trammel[1], Amy A. Simon-Miller[4], Barney J. Conrath[5], Peter J. Gierasch[5], Glenn S. Orton[2], Conor A. Nixon[6], Gianrico Filacchione[7], Patrick M. Fry[8], Thomas W. Momary[2]

[1] *Department of Physics, University of Houston, Houston, TX 77204, USA.*

[2] *Jet Propulsion Laboratory, Caltech, Pasadena, CA, 91109, USA.*

[3] *Dpto, Fisica Aplicada I, E.T.S. Ingenieria UPV/EHU, c/Alda. Urquijo s/n, 48013 Bilbao, Spain.*

[4] *NASA Goddard Space Flight Center, Greenbelt, MD 20771, USA.*

[5] *Department of Astronomy, Cornell University, Ithaca, NY 14853, USA.*

[6] *Department of Astronomy, University of Maryland, College Park, MD 20742, USA.*

[7] *INAF-IAPS, Istituto di Astrofisica e Planetologia Spaziali, Area di Ricerca di Tor Vergata, via del Fosso del Cavaliere, 100, 00133, Rome, Italy.*

[8] *Space Science and Engineering Center, University of Wisconsin, Madison, WI 53706, USA.*

* To whom all correspondence should be addressed. E-mail: lli7@uh.mail.edu

ABSTRACT

The emitted power of Jupiter and its meridional distribution are determined from observations by the Composite Infrared Spectrometer (CIRS) and Visual and Infrared Spectrometer (VIMS) onboard Cassini during its flyby en route to Saturn in late 2000 and early 2001. Jupiter's global-average emitted power and effective temperature are measured to be 14.10±0.03 Wm^{-2} and 125.57±0.07 K, respectively. On a global scale, Jupiter's 5-μm thermal emission contributes ~ 0.7±0.1% to the total emitted power at the global scale, but it can reach ~ 1.9±0.6% at 15°N. The meridional distribution of emitted power shows a significant asymmetry between the two hemispheres with the emitted power in the northern hemisphere 3.0±0.3% larger than that in the southern hemisphere. Such an asymmetry shown in the Cassini epoch (2000-01) is not present during the Voyager epoch (1979). In addition, the global-average emitted power increased ~ 3.8±1.0% between the two epochs. The temporal variation of Jupiter's total emitted power is mainly due to the warming of atmospheric layers around the pressure level of 200 mbar. The temporal variation of emitted power was also discovered on Saturn (Li et al., 2010). Therefore, we suggest that the varying emitted power is a common phenomenon on the giant planets.

1) INTRODUCTION

The absorbed solar radiance and the emitted thermal emission determine the energy budget of an astronomical body. For three of the four giant planets in our solar system (i.e., Jupiter, Saturn, and Neptune), large energy imbalances between the absorbed solar radiance and the emitted thermal emission were discovered and hence the internal heat was inferred. Such large energy imbalances and internal heat have important implications for atmospheric circulation and planetary formation/evolution, as reviewed in two related studies (Conrath et al., 1989; Hanel et al., 2003) and in our previous study of Saturn's emitted power (Li et al., 2010).

Previous observations of Jupiter (Ingersoll et al., 1975; Hanel et al., 1981; Pirraglia, 1984) have provided some important characteristics of the energy budget, the internal heat, and their meridional distributions. However, the temporal variability of the energy budget for Jupiter has not been explored mainly due to the limited observation set. Yet, it provides valuable clues for examining the time scale of internal heat referred from the theories of planetary formation/evolution (Smoluchowski, 1967; Salpeter, 1973; Flasar, 1973; Stevenson and Salpeter, 1977; Grossman et al., 1980; Guillot et al., 2004). In addition, the meridional distribution of energy budget and its temporal variation provide insights into atmospheric dynamics and general circulation (Pirraglia, 1984; Friedson and Ingersoll, 1987). The measurements of Jupiter's energy budget set important constraints on the heating/cooling rates as a function of altitude in the jovian atmosphere, following a similar study for the saturnian atmosphere (Perez-Hoyos and Sanchez-Lavega, 2006). The exploration of the heating/cooling rates and their temporal variation will help us study the atmospheric circulation and dynamics on Jupiter. As well, the temporal variation of the energy budget also provides one more perspective on Jupiter's climatology. The decadal-scale variation of cloud activity and the related convection has been characterized on Jupiter (Baines et al., 2007). Moist convection is inferred to be a prime transporter of internal heat on Jupiter (Gierasch et al., 2000; Ingersoll et al., 2000). Therefore, measurements of the temporal variation of the internal heat help determine if the decadal variation of convection and hence cloud variability acts as a valve that varies the flux from the interior of Jupiter and further adjusts possible climate change (Marcus, 2000).

The Cassini observations provide an opportunity to revisit the energy budget on Jupiter. Furthermore, the combination of the Cassini observations and the previous observations provides an opportunity to explore its temporal variability. This study is the first of a series of studies examining the temporal variability of the energy budget on Jupiter. In this study, we present the exploration of Jupiter's emitted power as determined by Cassini observations, and compare it with previous measurements from Pioneer/Voyager (Ingersoll et al., 1975; Hanel et al., 1981; Pirraglia, 1984). Observations from Earth-based and airborne telescopes are not included in this study because of the relatively large uncertainties and the discrepancies among them (please refer to Table 1 in Hanel et al., 1981 and Table I in Conrath et al., 1989). Note: planetographic latitude is used in this study. In addition, the solar longitude, which is defined as the angular distance along Jupiter's orbit around Sun measured from a reference point in the orbit (i.e., the zero of solar longitude at northern spring equinox), is used to track the different seasons.

2) METHODOLOGY

The methodology of computing a planet's emitted power (i.e., the emitted energy per unit time over a unit area) with the Cassini observations was introduced in our previous study of Saturn's emitted power (Li et al., 2010). The basic idea is that we will integrate recorded radiance over emission angle and wavelength to obtain Jupiter's emitted power.

In comparison to the on-orbit long-term (2004-) observations of Saturn, the Jupiter flyby observations by Cassini are somewhat limited in the coverage of emission angle. To fill the observational gaps in the coverage of emission angle, additional techniques (e.g., linear regression) are needed beyond the least-squares fit method (see Section 4). In addition, the thermal emission near 5 μm is significantly strong on Jupiter (Westphal, 1969), and is thus included in our computation of Jupiter's emitted power (Conrath et al., 1989).

Finally, the method of addressing the dependence of atmospheric radiance upon the emission angle is different between this Cassini study and the previous Voyager studies (Pirraglia, 1984, Ingersoll, 1990). In the Cassini analysis, the least-squares fit and the linear regression are used to fill the observational gaps in the emission angle (please see Section 4). Such a method does not require the knowledge of the temperature structure and chemical components of Jupiter's atmosphere. The Voyager observations has much less coverage in the emission angle than the coverage in the Cassini observations in the middle infrared (i.e., FP3 and FP4), so the method of the least-square fit does not work for filling the observations gaps in the Voyager observations. Instead, the dependence of the atmospheric radiance upon the emission angle was addressed by the radiative-transfer calculations with the retrieved atmospheric temperature and opacity (Hanel et al., 1981) in the previous Voyager studies (Pirraglia, 1984),(also see Section 4).

3) CASSINI OBSERVATIONS AND DATA PROCESSING

The measurements of Jupiter's emitted power are based on the Cassini observations obtained during the period of the Jupiter flyby, from October 1, 2000 to March 22, 2001. We use the observations from two instruments. The Composite Infrared Spectrometer (CIRS) measures the great majority of the outgoing thermal emission of Jupiter with wavelengths from 7 to 1000 μm. The Visual and Infrared Mapping Spectrometer (VIMS) records the 5-μm thermal emission. The two instruments and the corresponding data processing are described below.

3.1) Cassini/CIRS Observations

The CIRS instrument (Flasar et al., 2004a) acquires Jupiter's spectra in three focal planes: FP1, FP3, and FP4, covering 10-600 cm^{-1}, 600-1050 cm^{-1}, and 1050-1430 cm^{-1}, respectively. With all three focal planes, CIRS measures Jupiter's thermal emission in wavenumber over 10 to 1430 cm^{-1} (i.e., 7 to 1000 μm) with adjustable spectral resolutions from 0.5 to 15.5 cm^{-1}. In this study, we analyze Jupiter's spectra with two resolutions (i.e., 2.8 cm^{-1} and 0.5 cm^{-1}), that provide the best spatial coverage. Data with other spectral resolutions are not included because their spatial coverage is negligible compared the spectra with resolutions of 2.8 cm^{-1} and 0.5 cm^{-1}.

Figure 1 displays a typical spectrum of Jupiter recorded by CIRS. The theoretical framework introduced in previous studies (Conrath et al., 1989; Li et al., 2010) shows that the outgoing thermal emission is determined by measurements of outgoing radiance at different emission angles and different latitudes. Therefore, we process the CIRS spectra into 2-dimensional (latitude × emission angle) wavenumber-integrated radiance (Li et al., 2010) with a resolution of 1° in both latitude and emission angle. Here, we average all CIRS observations within each 1° latitude bin based on the center latitudes of spectra. The spatial resolution of processed data (1°)

is higher than the spatial resolution of the raw CIRS observations (~ 3-40°), which is determined by the field of view of CIRS and the distance between Jupiter and Cassini. Figure 2 shows the final data products: zonal-mean wavenumber-integrated radiance in the plane of latitude and emission angle recorded by FP1, FP3, and FP4, respectively. Figure 2 suggests that Jupiter's radiance varies not only in the direction of latitude about also in the direction of emission angle. The variation of Jupiter's radiance along the direction of longitude is generally less than 3%, which is not shown in Fig. 2, but is accounted in the estimates of the uncertainty of Jupiter's emitted power (please see Section 4).

3.2) Cassini/VIMS Observations

The shortest wavelength (i.e., largest wavenumber) of the CIRS spectra is ~ 7 μm (i.e., ~ 1430 cm^{-1}). Therefore, the CIRS observations do not record the 5-μm thermal emission spectral component of Jupiter. This range is covered by another Cassini infrared instrument – VIMS. The VIMS instrument is a color camera that acquires spectral cubes encompassing 352 different wavelengths between 0.35 μm and 5.1 μm (Brown et al., 2004). It is designed to measure scattered and emitted light from surfaces and atmospheres, with emphasis on covering a broad spectral domain with moderate spatial resolution.

In this study, we use 11 full-disk VIMS observations recorded on January 7-8, 2001, about eight days after the closest approach to Jupiter. The VIMS observations from 4.4 μm to 5.1 μm are utilized to explore the emitted power of the 5-μm thermal band, which has a spectral range of 4.4-5.6 μm (see Section 4.2). All global VIMS images at different wavelengths are well navigated and calibrated by the VIMS Operations Team based at the University of Arizona, following techniques discussed by Barnes et al., (2007). The raw 5-μm VIMS global images are generally stored in units of I/F, the ratio of recorded radiance to the known total incident solar radiance (Thekaekara, 1973). Panel A of Fig. 3 displays one example of the 5-μm VIMS global images in such units. With the known total incident solar radiance, we can convert the recorded VIMS radiance from I/F to a general radiance unit (panel B). To obtain the intrinsic thermal emission of Jupiter around 5 μm, we eliminate the solar scattering component by analyzing only the night-side portions of these VIMS images (panel C).

4) RESULTS

4.1) Emitted Power in the Wavenumber Range of CIRS

As is evident in Fig. 2, the CIRS observations do not occupy the whole plane of latitude and emission angle. In order to calculate the emitted power at each latitude from integration of the radiance over the entire range of emission angle (Li et al., 2010), it is necessary to fill the gaps in the observed emission angle. Following the method used in our study of Saturn's emitted power (Li et al., 2010), wherein the interpolation/extrapolation from the existing observations was accomplished with a technique of least-squares fit (Bevington and Robinson, 2003), we fill the observational gaps in FP3 and FP4 (panels B and C). Different polynomials of emission angle were tried for the best fitting (i.e., the fitting with the least fitting residual). Here, the fitting residual is defined as the difference between the fitting value and observational data (i.e., fitting value-observational data). We find that the following first-order (degree) polynomial has the best fitting results for observed radiance by FP3 and FP4:

$$I(\delta) = c_1 \cos\delta + c_2 \qquad (1)$$

where δ is emission angle. The parameters c_1 and c_2 are coefficients that are fitted and determined by the observed radiance. Figure 4 shows some example fits with Eq. (1) at different latitudes for the focal planes FP3 and FP4, which suggests that the least-squares fit works well for the existing observations.

The fitting function Eq. (1) with the known coefficients (c_1 and c_2) is used to fill the observational gaps in emission angle for the radiance recorded by FP3 and FP4 (panels B and C in Fig. 2). The radiance after filling the observational gaps is shown in panel A of Figs. 5 and 6. Panel B of Figs. 5 and 6 is the ratio of fitting residual to the raw radiance for these observational points, which highlights the difference between the observations and the fitting results. Panel B shows that the ratio is mostly less than 5% at all latitudes. The fitting residual is further utilized in the following estimates of the uncertainty of filling observational gaps.

However, the same technique does not work for the FP1 observations, because the coverage of observed FP1 radiance is very limited (panel A of Fig. 2). For a planetary atmosphere, the thermal radiances at different wavenumbers are correlated with each other. Such a correlation can be utilized to estimate the radiance at the unmeasured wavenumbers from the radiance at the measured wavenumbers (Ingersoll et al., 1975). Here, we estimate the unmeasured FP1 radiance (10-600 cm^{-1}) from the FP3 radiance (600-1050 cm^{-1}), which has much better spatial coverage.

First, we examine the correlation between the FP1 radiances and the FP3 radiance. Our experiments show that there is good correlation between the FP1 radiances and the FP3 radiances with the each latitude bin. Fig.7 displays the scatter plots for these latitude bins with the relatively more simultaneous observations from FP1 and FP3, which are based on panels A and B of Fig. 2. The good correlation between the FP1 radiances and the FP3 radiances makes it possible to regress the FP1 radiances from the FP3 radiances. Figure 8 shows the ratios of the FP1 radiances to the FP3 radiances (i.e., FP1/FP3). This figure suggests that the ratio FP1/FP3 does not vary significantly with emission angle, probably because the FP1 and FP3 radiances have the same variation with emission angle (Fig. 2). Figure 9 further presents the zonal mean value and the standard deviation of FP1/FP3 within each latitude bin in Fig. 8. The ratio of the standard deviation (panel B) to the zonal mean value (panel A) is less than 1.5% (panel C), which indicates that there is no significant variation along the direction of emission angle. Figure 8 also shows that there are some banded structures of the radiance ratio FP1/FP3 in the meridional direction. The banded structures in Fig. 8 are correlated to the banded structures in the radiance recorded by FP3 (panel A of Fig. 5), which are further related to the banded structures of clouds on Jupiter.

The correlation of the banded structures between the ratio FP1/FP3 (Fig. 8) and the FP3 radiance (Fig. 5) can be used to explore the FP1 radiance. Panel A of Fig. 10 shows the zonal mean of the FP3 radiance within each latitude bin, which is based on panel A of Fig. 5. The structures of the FP3 radiance in the meridional direction have similar shape as the structures of the ratio FP1/FP3 (panel A of Fig. 9) but with opposite direction, which suggests that the FP3 radiance is dominant in the ratio FP1/FP3. Therefore, we can utilize the linear regression of the FP3 radiance to estimate the ratio FP1/FP3 in these latitudes where the FP1 observations are not available. Panel B of Fig. 10 shows the comparison between the linearly regressed ratio FP1/FP3 and the observed ratio FP1/FP3. The correlation coefficient between the observed FP1/FP3 and the regressed FP1/FP3 is beyond 0.99, which suggests that the linear regression works well.

Based on the fitting results of the FP3 radiance (panel A of Fig. 5) and the regressed ratio FP1/FP3 (panel B of Fig. 10), we can estimate the FP1 radiance in the plane of latitude and emission angle, which is displayed in panel A of Fig. 11. Panel B of Fig. 11 shows the ratio of the regression residual (i.e., difference between the regressed FP1 radiance and the raw FP1 radiance) to the raw FP1 radiance. The ratio in panel B is basically less than 2%, which suggests that the linear regression of the FP3 radiance works well for estimating the FP1 radiance.

After filling the observational gaps in the thermal radiance recorded by the three CIRS focal planes (panel A of Figs. 5, 6, and 11), we can estimate Jupiter's emitted power. Figure 12 shows the meridional profile of Jupiter's emitted power in the CIRS spectral range (10-1430 cm^{-1} ~ 7-1000 μm). The uncertainties shown in Fig. 12 include three sources: 1) the uncertainty related to the CIRS calibration; 2) the uncertainty related to the filling of observational gaps in the emission angle along the each latitude; and 3) the standard deviation of multiple CIRS observations with different longitudes with the same latitude and emission angle. The first uncertainty source, which is related to the CIRS calibration by removing the radiance of the background, can be estimated by the spectra of deep space (Li et al., 2010). The second uncertainty source is related to the filling of observational gaps in FP1 and FP3/4 by the least-squares fit and the linear regression, respectively. The method of estimating the uncertainties related to the filling of the observational gaps by FP3 and FP4 by the least-squares fit, which is based on the fitting residual (i.e., fitting value-observational data), has been discussed in our previous Saturn paper (Li et al., 2010). Along the each latitude, the standard deviation of the fitting residual at these emission angles with available FP3/FP4 data is used to estimate the uncertainty of the fitting radiances at these emission angles, where the FP3/FP4 raw data are not available (i.e., observational gaps) (Li et al., 2010). As for the uncertainty related to the regressed FP1 radiance by the linear regression of the FP3 radiance, we use the standard deviation of the regression residual (panel B of Fig. 11) to estimate the uncertainty at these latitudes where the FP1 raw data are available. Based on the existing estimates of the FP1 uncertainty, we use a linear interpolation/extrapolation to estimate the FP1 uncertainty in these latitudes where the raw FP1 observations are not available. The second uncertainty, which has a magnitude $10^{-1}Wm^{-2}$, is two-order of magnitude larger than the first uncertainty, which has a magnitude $10^{-3}Wm^{-2}$. The third uncertainty, which is the standard deviation of multiple CIRS measurements at different longitudes with the same latitude and emission angle, has the same magnitude as that of the second uncertainty. Considering that the three uncertainty sources are independent, we combine them by the square root of the sum of the squares of the individual uncertainties (Daley, 1991).

4.2) Emitted Power From the 5-μm thermal Emission

We use the VIMS observations to measure Jupiter's emitted power around 5 μm, which is outside of the spectral range of the CIRS spectra. The complete 5-μm thermal emission band covers the spectral range 4.4-5.6 μm (Irwin, 1999), longer than the spectral range of 4.4-5.1 μm covered by VIMS. To derive the power over the full 5-μm thermal band, we fist integrate VIMS spectra over the spectral range of 4.4-5.1 μm. We then explore the ratio of wavelength-integrated radiance between the VIMS spectral range (i.e., 4.4-5.1 μm) and the complete spectral range (i.e., 4.4- 5.6 μm). Finally, the VIMS observations and the radiance ratio between 4.4-5.1 μm and 4.4- 5.6 μm are combined together to estimate the total emitted power from the 5-μm thermal band.

Our examination (not shown) and the previous study (Roos-Serote and Irwin, 2006) both suggest that the magnitude of Jupiter's 5-μm spectra varies with time and space but the shape of the spectra basically remains unchanged. Therefore, it is reasonable to assume that the ratio of wavelength-integrated radiance between the VIMS spectral range (i.e., 4.4-5.1 μm) and the complete spectral range (i.e., 4.4- 5.6 μm) does not change significantly with time and space on Jupiter. Therefore, we can estimate the total 5-μm thermal emission over 4.4- 5.6 μm from the known VIMS measurements over 4.4-5.1 μm if we know the ratio between them.

We use the complete 5-μm spectra from the Infrared Interferometer Spectrometer (IRIS) on Voyager to get the ratio of wavelength-integrated radiance between the VIMS spectral range (4.4-5.1 μm) and the complete spectral range (4.4-5.6 μm). Figure 13 shows the comparison of the global-average spectrum between Cassini/VIMS and Voyager/IRIS, which suggests that the 5-μm spectra from IRIS and VIMS have basically the same structures. It should be mentioned that some fine spectral structures shown in the IRIS spectrum do not show in the VIMS spectrum, because the spectral resolution is much higher in IRIS (~ 0.005 μm) than in VIMS (~ 0.017 μm). We use the complete IRIS spectrum to compute the ratio of wavelength-integrated radiance between the VIMS spectral range (i.e., 4.4-5.1 μm) and the complete spectral range (i.e., 4.4- 5.6 μm), which has a value of 0.711.

We divide the wavelength-integrated radiance from the VIMS measurements (4.4-5.1 μm) by the ratio to estimate the total emitted power from the thermal emission around 5 μm, which is shown in Fig. 14. The uncertainty (error-bar) shown in Fig. 14 is based on two factors: 1) the absolute calibration error and 2) the standard deviation of multiple VIMS measurements within each latitude bin (1°) and within the two-day period (January 7-8, 2001 with 11 global observations). For the first factor, we refer to the study by Buratti et al., (2010), in which the absolute error of the VIMS data was estimated to be 5-10% of the recorded VIMS radiance. Here, we use the average value (i.e., 7.5%) to represent the absolute calibration error. The second uncertainty factor, which is related to the longitudinal and temporal variation of the 5-μm radiance, can reach ~ 50% of the total 5-μm radiance at some latitudes. Figure 14 shows the strongest 5-μm thermal emission exists in the latitude band around 15° in the two hemispheres. The global-average emitted power of the 5-μm thermal emission is 0.09±0.01 Wm^{-2}, which is ~ 0.7±0.1% of Jupiter's total emitted power ~ 14.10±0.02 Wm^{-2} (see Section 4.3). The strongest 5-μm thermal emission around 15°N can reach ~ 1.9±0.6% of Jupiter's total emitted power at this latitude.

4.3) Total Emitted Power of Jupiter

Thermal radiance outside the spectral range of CIRS (10-1430 cm^{-1}) and the 5-μm emission band (1800-2250 cm^{-1}) has negligible contribution to the total emitted power of Jupiter (Conrath et al., 1989), and so it is not considered in this study. Thus, we estimate Jupiter's emitted power and effective temperature at different latitudes by simply adding the values in Fig. 12 and Fig. 14. The corresponding uncertainty is estimated by the square root of the sum of the squares of the uncertainties from the CIRS measurements (Fig. 12) and the VIMS measurements (Fig. 14), because the two uncertainties are independent (pages 42-43 in Bevington and Robinson, 2003).

The meridional distribution of Jupiter's total emitted power is displayed in Fig. 15, which shows an asymmetry of emitted power/effective temperature between the northern and southern hemispheres. There are very limited observations in the polar region beyond 77° in the Jupiter flyby mission by Cassini, so we cannot estimate the emitted power in the polar region. Assuming the emitted power at the unmeasured polar region (77-90° S/N) has the same value and uncertainty as the value at 76° S/N, we can evaluate the hemispheric average of emitted power and the corresponding effective temperature, which are shown in Table 1. Table 1 shows that the emitted power and effective temperature are higher in the northern hemisphere (NH) than in the southern hemisphere (SH) by $0.41\pm0.04 Wm^{-2}$ ($3.0\pm0.3\%$) and $0.92\pm0.09K$ ($0.7\pm0.1\%$), respectively.

In addition to the asymmetry between the two hemispheres, there are some relatively small-scale oscillations of emitted power/effective temperature shown in Fig. 15, which are related to the temperature structures in Jupiter's troposphere. The tropical temperature shown in this figure was retrieved from the Cassini/CIRS spectra at a wavenumber range of 600-690 cm^{-1} (Flasar et al., 2004b, Simon-Miller et al., 2006). Figure 16 shows that the profile of effective temperature sits between the 330-mbar profile and the 420-mbar profile of atmospheric temperature. Therefore, the weighting function of the outgoing thermal radiance peaks around the two pressure levels. Figure 16 also shows that the structures of effective temperature in the two hemispheres are more similar to the temperature profiles of the shallower atmosphere (170-270 mbar), suggesting that they also contribute to Jupiter's outgoing thermal radiance. Figure 16 suggests that Jupiter's emitted power (i.e., effective temperature) is related to the atmospheric temperature. However, the asymmetry between the two hemispheres, which is shown in Jupiter's emitted power (Fig. 15), does not significantly show in the atmospheric temperature (Fig. 16). Therefore, we suggest that there are other mechanisms (e.g., spatial distribution of cloud/haze) possibly influencing the meridional distribution of Jupiter's emitted power.

The meridional distribution of emitted power was also measured in some previous studies (Pirraglia, 1984; Ingersoll, 1990). Pirraglia (1984) measured the meridional profile of emitted power with the flyby observations by Voyager 1. The meridional profile in the paper by Ingersoll (1990) was combined from the Voyager observations in the low and middle latitudes (Pirraglia, 1984) and the Pioneer observations in the high latitudes (Ingersoll et al., 1975). There are no multiple focal panels in the Voyager/IRIS (Hanel et al., 1980), and the observations recorded by the Voyager/IRIS have very limited coverage in the plane of latitude and emission angle (Hanel et al., 1981; Pirraglia, 1984). Therefore, the method we used in this study for computing Jupiter's emitted power from the Cassini/CIRS observations (i.e., interpolating the FP3/FP4 observations and regressing the FP1 observations from the FP3/FP4 observations) does not work for the Voyager/IRIS observations. Instead, a method, in which the gaps in the emission angle are considered by the radiative-transfer calculations with the given atmospheric temperature and opacity profiles (Hanel et al., 1981, 1983), was used in the analysis of the Voyager observations (Pirraglia, 1984; Ingersoll et al., 1990). The comparison between the limited observations and the radiative-transfer calculations (Pirraglia, 1984) suggests that the above method also works well under the condition of lacking the necessary coverage of latitude and emission angle.

Figure 17 displays the profile of emitted power from the Voyager observations in 1979, compared to the profile from the Cassini observations in 2000-01. The uncertainty in the

Voyager profile comes from the measurements by Pirraglia (1984). In the study by Pirraglia (1984), the standard deviation of multiple measurements within each latitude bin, corresponding to the zonal mean emitted power along the longitude direction, was taken as the uncertainty. Such an estimate of uncertainty does not account for the uncertainty related to the calibration of the Voyager/IRIS, which has a magnitude $10^{-2}Wm^{-2}$ (Hanel et al., 1981). However, the uncertainty due to the calibration is approximately one-order of magnitude smaller than the standard deviation shown in Fig. 17 ($\sim 10^{-1}Wm^{-2}$). Therefore, it does not significantly vary the uncertainty estimated by Pirraglia (1984). The uncertainty of the Cassini profile is based on more uncertainty sources from the CIRS measurements (Section 4.1) and the VIMS measurements (section 4.2). The latitude bin in the Cassini measurements (i.e., 1°) is narrower than the latitude bin in the Voyager/IRIS measurements (i.e., 4-5°) (Pirraglia, 1984). The standard deviation of multiple measurements within each latitude bin in the previous study (Pirraglia, 1984) is roughly three times of that in our study. Figure 17 shows that the total uncertainty considering more sources in our study is still smaller than the uncertainty in the Voyager measurements by Pirraglia (1984).

Figure 17 shows significant difference between the two profiles, which is larger than the measurement uncertainty at most latitudes. In particular, the asymmetry of emitted power/effective temperature between the two hemispheres, which is evident in the Cassini observations, does not appear in the Voyager measurements. Table 2 shows the comparison of global-average emitted power and effective temperature between the current measurements by Cassini and the previous measurements by Voyager 1 (Hanel et al., 1981). In addition, the global-average value from the measurements by Pioneer (Ingersoll et al., 1975), which have relatively larger uncertainty, is also listed in Table 2. The differences of emitted power and effective temperature between Voyager and Cassini are larger than the corresponding uncertainties. From the Voyager epoch to the Cassini epoch, the global-average emitted power and effective temperature increased by 0.51±0.14 Wm^{-2} (3.8±1.0%) and 1.17±0.31 K (0.9±0.2%), respectively. When exploring the temporal variation of the global values between the two epochs, the known uncertainty sources including data calibration are considered in the measurements by Voyager (Hanel et al., 1981) and by Cassini (this study). It should be mentioned that it is still possible that there are unknown calibration issues affecting the measurements in the two epochs.

Why did Jupiter's emitted power and effective temperature change with time? We first examine if there is any variation in the altitude of the atmospheric layers involving the outgoing thermal radiance on Jupiter. Figure 18 displays the comparison of the effective temperature and the atmospheric temperature in the Voyager epoch. The tropospheric temperature shown in Fig. 18 comes from the retrievals of the Voyager/IRIS spectra in the spectral intervals 320-430 cm^{-1} and 520-600 cm^{-1} (Simon-Miller et al., 2006). The comparison shows that the profile of effective temperature sits between the 310-mbar profile and 410-mbar profile of atmospheric temperature, which suggests that the atmospheric layers around the two pressure levels contribute significantly to the outgoing thermal radiance on Jupiter. The difference between the profile of effective temperature and the profiles of atmospheric temperature at 310 mbar and 410 mbar suggests that the atmospheric layers at other pressure levels also contribute to Jupiter's outgoing thermal radiance. The comparison between Fig. 16 (Cassini profiles) and Fig. 18 (Voyager profiles) further suggests that the peak of the weighting function of the outgoing thermal radiance did not change significantly from the Voyager epoch to the Cassini epoch. Therefore, we rule out the varying weighting function of outgoing thermal radiance as the main physics behind the temporal variation of emitted power/effective temperature shown in Fig. 17.

Jupiter's emitted power is directly related to the temperature of atmospheric layers, so the temporal variation of emitted power (Fig. 17) means that there is the corresponding variation in the atmosphere temperature. Figure 19 is the comparison of Jupiter's temperature in the upper troposphere between the Voyager epoch and the Cassini epoch. Figure 19 suggests that the warming of the atmospheric layers around 200 mbar contributes to the increased emitted power in the latitude bands outside of the equatorial region (i.e., 10°N-10°S) (Fig. 17). In addition, the cooling of the atmospheric layers between 50 mbar and 500 mbar in the equatorial region explains the decreased emitted power in that region from the Voyager epoch to the Cassini epoch. Much of this cooling was noted immediately after the Voyager encounters (Orton et al., 1994) and was even detectable between Voyagers 1 and 2.

The temporal variation of the atmospheric temperature provides one explanation for the varied emitted power from Voyager to Cassini. The continuous observations from 1980 to 1993 (Orton et al., 1994) and from 1979 to 2001 (Simon-Miller et al., 2006) suggest that Jupiter's tropospheric temperature changed gradually from the Voyager epoch to the Cassini epoch (i.e., ~ 2 Jovian years), with little obvious seasonal or short-term variation. In other words, there is probably long-term variation (e.g., inter-annual variation) in Jupiter's tropospheric temperature. As a result, Jupiter's emitted power and effective temperature, which are mainly determined by

Jupiter's tropospheric temperature, probably have a corresponding inter-annual variability existing in the temporal variation shown in Fig. 18.

Next, we explore the physics behind the temporal variation of the atmospheric temperature and hence the emitted power from the Voyager epoch to the Cassini epoch. First, let us take a look at the solar flux on Jupiter. The average solar longitude of the Voyager observations was 174.5°. The average solar longitude of the Cassini mission in 2000-01 was 110.5°. Figure 20 shows the seasonal variation of solar flux from the Voyager epoch (i.e., solar longitude ~ 174.5°; northern late summer) to the Cassini epoch (i.e., solar longitude ~ 110.5°; northern early summer). On Earth, the temporal variation in the meridional distribution of solar flux is the main driver of the seasonal variation of atmospheric temperature. However, the temporal variation in the meridional distribution of solar flux (Fig. 19) is probably not the main driver for the temporal variation of atmospheric temperature (Fig. 18), mainly because of the relativity small temporal variation of solar flux on Jupiter due to its small orbital obliquity (i.e., 3°). The comparison between Fig. 19 and Fig. 20 also suggests that there is no direct relationship between the varying solar flux and the temporal variation of atmospheric temperature. First, the increased solar flux in the NH cannot explain the cooling of atmospheric temperature between 50 mbar and 100 mbar (Fig. 19). Second, the decreased solar flux in the high latitudes of the SH cannot explain the increased atmospheric temperature around 200 mbar in the same latitudes. Finally, the smooth profile of solar flux and its temporal variation cannot explain the temporal variation of atmospheric temperature at the small length-scale (i.e., a few latitude degrees) in Fig. 19. Therefore, the above analyses suggest that there are probably other mechanisms to drive the temporal variation of tropospheric temperature, emitted power, and effective temperature on Jupiter.

The second possible driving force is the decadal-scale variability of cloud cover on Jupiter (Baines et al., 2007). The variation of cloud cover will redistribute the solar flux on Jupiter, and hence modify the thermal structure and the related emitted power. The third possible driving force is wave activity. The atmospheric waves, which are thought to be the mechanism of the Quasi-Biennial Oscillation (Lindzen and Holton, 1968, Baldwin et al., 2001) and sudden warming (Baldwin and Dunkerton, 1989) in the stratosphere of Earth, can also drive the large-scale variation of temperature and wind fields. Likewise, such a mechanism works for the quasi-quadrennial oscillation on Jupiter (Leovy et al., 1991; Orton et al., 1991; Friedson et al., 1999; Li and Read, 2000). The wave-driven oscillations mainly exist in the stratospheres of planetary atmospheres, but we cannot rule out the roles of waves (Porco et al., 2003; Li et al., 2006) and other dynamical processes (e.g., vortices, eddies and storms) in modifying the large-scale thermal structure in the troposphere of Jupiter.

5) CONCLUSION AND DISCUSSION

Jupiter's spectra recorded by Cassini CIRS and VIMS during the period of 2000-01 are systematically analyzed to evaluate the emitted power and effective temperature of Jupiter. Our analysis indicates that in the Cassini epoch the global-average emitted power and effective temperature were 14.10±0.03 Wm^{-2} and 125.57±0.07 K, respectively. Jupiter's 5-μm thermal emission, which is produced near the 6-bar level and is modulated by relatively deep cloud layers of ammonia hydrosulfide (i.e., ~ 1-3 bar), contributes ~ 0.7±0.1% to the total emitted power at the global scale. However, the strongest 5-μm thermal emission around 15°N can reach ~ 1.9±0.6% of the total emitted power at that latitude. The emitted power was 3.0±0.3% higher in the NH than in the SH in the Cassini epoch. Such an asymmetry was not present in the Voyager epoch. Furthermore, Jupiter's emitted power increased ~ 3.8±1.0% on a global scale from the Voyager epoch to the Cassini epoch.

Our analyses of atmospheric temperature reveal that the temporal variation of emitted power from the Voyager epoch to the Cassini epoch is mainly due to the warming of atmospheric layers around 200 mbar. The mechanisms of the temporal variation of tropopheric temperature and the related emitted power are unclear. We suggest that the temporal variation of cloud cover and some dynamical processes (e.g., waves, vortices, eddies, and storms) are possible mechanisms to drive the temporal variation of the large-scale atmospheric temperature and hence the temporal variation of emitted power on Jupiter, but long-term continuous observations and more theoretical studies are needed to understand the temporal variation in the jovian atmosphere. On the other hand, the varying emitted power implies that the energy budget and its meridional distribution probably change with time on Jupiter. The potentially varying energy budget will inversely modify the atmospheric structures, large-scale circulation, and dynamical processes. Therefore, the coupling between the varying energy budget and the evolving atmospheric structure/dynamics, which makes Jupiter's atmospheric system very complicated, should be considered in the future exploration.

Our follow-up studies, which are based on observations of reflected solar radiance in the visible band from the Imaging Science Subsystem (ISS) and VIMS on Cassini, will help us measure the absorbed solar radiance on Jupiter during the Cassini epoch. Combining measurements of the emitted thermal radiance and absorbed solar energy, we can determine the energy budget and hence internal heat in the Cassini epoch. As well, Cassini measurements can be compared with previous measurements (i.e., Pioneer and Voyager) to detect and characterize the temporal variation of the energy budget and internal heat on Jupiter.

References

Baines, K. H., and 18 colleagues, 2007. Polar lightning and decadal-scale cloud variability on Jupiter, Science 318, 226-229.

Barnes, J. W., R. H. Brown, L. Soderblom, B. J. Buratti, C. Sotin, S. Rodriguez, S. L. Mouelic, K. H. Baines, R. Clark, P. Nicholson, 2007. Global-scale surface spectral variation on Titan seen from Cassini/VIMS. Icarus 186, 242-258.

Baldwin and Dunkerton, 1989. The stratospheric major warming of early December 1987. J. Atmos. Sci. 46, 2863-2884.

Baldwin, M. P., and 14 colleagues, 2001. The quasi-biennial oscillation. *Reviews of Geophysics* 39, 179-229.

Bevington, P. R., and D. K. Robinson, 2003. Data reduction and error analysis for the physical sciences, third edition. McGraw-Hill, New York.

Brown, R. H., and 20 colleagues, 2004. The Cassini visual and infrared mapping spectrometer (VIMS) investigation, Space Sci. Rev. 115, 111-168.

Buratti, B. J., J. M. Bauer, M. D. Hicks, J. A. Mosher, G. Filacchione, T. Momary, K. H. Baines, R. H. Brown, R. N. Clark, P. D. Nicholson, 2010. Cassini spectra and photometry 0.25-5.1 μm of the small inner satellites of Saturn. Icarus 206, 524-536.

Conrath, B. J., R. A. Hanel, R. E. Samuelson, 1989. Thermal Structure and Heat Balance of the Outer Planets. In Origin and Evolution of Planetary and Satellite Atmospheres edited by Atreya, S. K., J. B. Pollack, and M. S. Matthews, The University of Arizona Press, Arizona.

Daley, R., 1991. Atmospheric data analysis. Cambridge University Press, Cambridge.

Flasar, F. M., 1973. Gravitational energy sources in Jupiter. Astrophys. J. 186, 1097-1106.

Flasar, F. M., and 45 colleagues, 2004a. Exploring the Saturn system in the thermal infrared: The Composite Infrared Spectrometer. Space Sci. Rev. 115, 169–297.

Flasar, F. M., and 39 colleagues, 2004b. An intense stratospheric jet on Jupiter. Nature 427, 132-135.

Friedson, A.J., 1999. New observations and modeling of a QBO-like oscillation in Jupiter's stratosphere. Icarus 137, 34–55.

Friedson, J., A. P. Ingersoll, 1987. Seasonal meridional energy balance and thermal structure of the atmosphere of Uranus: a radiative-convective-dynamical model. Icarus 69, 135-156.

Gierasch, P. J., A. P. Ingersoll, D. Banfield, S. P. Ewald, P. Helfenstein, A. Simon-Miller, A. Vasavada, H. H. Breneman, D. A. Senske, and Galileo Imaging Team, 2000. Observation of moist convection in Jupiter's atmosphere. Nature 403, 628-630.

Grossman, A. S., J.B. Pollack, R. T. Reynolds, A. L. Summers, 1980. The effect of dense cores on the structure and evolution of Jupiter and Saturn. *Icarus* 42, 358-379.

Guillot, T., D. J. Stevenson, W. B. Hubbard, and D. Saumon, 2004. The Interior of Jupiter. In Jupiter: The planet, Satellites, and Magnetosphere edited by Bagenal, F., T. Dowling, and W. Mckinnon, Cambridge University Press, Cambridge.

Hanel, R. A., B. J. Conrath, L. W. Herath, V. G. Kunde, J. A. Pirraglia, 1981. Albedo, internal heat, and energy-balance of Jupiter – preliminary results of the Voyager infrared investigation. J. Geophy. Res. 86, 8705-8712.

Hanel, R. A., Conrath, B. J., Jennings, D. E., Samuelson, R. E, 2003. Exploration of the solar system by Infrared Remote Sensing. Cambridge University Press, New York.

Ingersoll, A. P., G. Munch, G. Neugebauer, D. J. Dineer, G. S. Orton, B. Schupler, M. Schroeder, S. C. Chase, R. D. Ruiz, L. M. Trafton, 1975. Pioneer 11 infrared radiometer experiment – global heat balance of Jupiter. Science 188, 472-473.

Ingersoll, A. P., 1990. Atmospheric dynamics of the outer planets. Science 248, 308-315.

Ingersoll, A. P., P. J. Gierasch, D. Banfield and A. R. Vasavada 2000. Moist convection as an energy source for the large-scale motions in Jupiter's atmosphere. Nature 403, 630-632.

Irwin, P. G. J., 1999. Cloud structure and composition of Jupiter's atmosphere. Surveys in Geophysics 20, 505-535.

Irwin, P.G.J., A. L. Weir, S. E. Smith, F. W. Taylor, A. L. Lambert, S. B. Calcutt, P. G. Cameron-Smith, R. W. Carlson, K. Baines, G. S. Orton, P. Drossart, T. Encrenaz, and M. Roos-Serote, 1998. Cloud structure and atmospheric composition of Jupiter retrieved from Galileo real-time spectra. *J. Geophys. Res.* **103**, 23,001–23,021.

Leovy, C.B., A. J. Friedson, G. S. Orton, 1991. The quasi-quadrennial oscillation of Jupiter's equatorial stratosphere. Nature 354, 380-382.

Li L., A. P. Ingersoll, A. R. Vasavada, A. A. Simon-Miller, R. K. Achterberg, S. P. Ewald, U. A. Dyudina, C. C. Porco, R. A. West, F. M. Flasar, 2006. Waves in Jupiter's atmosphere observed by the Cassini ISS and CIRS instruments, Icarus 185, 416-419.

Li, L., B. J. Conrath, P. J. Gierasch, R. K. Achterberg, C. A. Nixon, A. A. Simon-Miller, F. M. Flasar, D. Banfield, K. H. Baines, R. A. west, A. P. Ingersoll, A. R. Vasavada, A. D. Del Genio, C. C. Porco, A. A. Mamoutkine, M. E. Segura, G. L. Bjoraker, G. S. Orton, L. N. Fletcher, P. G.

J. Irwin, P. L. Read, 2010. Emitted power of Saturn. Journal of Geophysical Research - Planet, 115, art. No. E11002. With NASA feature story titled "Saturn is on a cosmic dimmer switch".

Li, X., P. L. Read, 2000. A mechanistic model of the quasi-quadrennial oscillation in Jupiter's stratosphere. Planet. Space Sci. 48, 637– 669.

Lindzen, R. S., and J. R. Holton, 1968. A theory of quasi-biennial oscillation, J. Atmos. Sci. 25, 1095-1107.

Marcus, P. S., 2004. Prediction of a global climate change on Jupiter. Nature 428, 828-831.

Orton, G., A. Friedson, J. Caldwell, H. Hammel, K. Baines, J. Bergstrahl, T. Martin, M. Malcolm, R. West, W. Golisch, D. Griep, C. Kaminski, A. Tokunaga, R. Baron, M. Shure, 1991. Thermal maps of Jupiter: Spatial organization and time dependence of stratospheric temperatures, 1980–1991. Science 252, 537–542.

Orton, G. S., and 18 colleagues, 1994. Spatial organization and time dependence of Jupiter's tropospheric temperatures, 1980-1993. Science 265, 625-631.

Perez-Hoyos, S., A. Sanchez-Lavega, 2006. Solar flux in Saturn's atmosphere: penetration and heating rates in the aerosol and cloud laygers. Icarus 180, 368-278.

Pirraglia, J. A., 1984. Meridional energy balance of Jupiter. Icarus 59, 169-176.

Porco, C., and 23 co-authors, 2003. Cassini imaging of Jupiter's atmosphere, satellites, and rings. Science 299, 1541–1547.

Porco, C. C., and 19 colleagues, 2004. Cassini Imaging Science: Instrument characteristics and anticipated scientific investigations at Saturn, Space Sci. Rev. 115, 363-497.

Roos-Serote, M. P. G. J. Irwin, 2006. Scattering properties and location of the jovian 5-micron absorber from Galileo/NIMS limb-darkening observations. Journal of Quantitative Spectroscopy and Radiative Transfer 101, 448-461.

Salpeter, E., 1973. On convection and gravitational layering in Jupiter and stars of low mass. Astrophys. J. 181, L83-L86.

Simon-Miller, A. A., B. J. Conrath, P. J. Gierasch, G. S. Orton, R. K. Achterberg, F. M. Flasar, B. M. Fisher, 2006. Jupiter's atmospheric temperatures: from Voyager IRIS to Cassini CIRS. Icarus 180, 98-112.

Smoluchowski, R., 1967. Internal structure and energy emission of Jupiter. Nature 215, 691-695.

Stevenson, D. J., and E. E. Salpeter, 1977. The dynamics and helium distributions in hydrogen-helium planets. Astrophys. J. Suppl. 35, 239-261.

Thekaekara, M. P., 1973. Solar energy outside the Earth's atmosphere. Solar Energy 14, 109-127.

Westphal, J. A., 1969. Observations of localized 5-mircron radiation from Jupiter. The Astrophysical Journal 157, L63-L64.

Figure Captions

Figure 1. Jupiter's combined spectrum based on the three spectra obtained by FP1, FP3, and FP4. The combined spectrum, which was recorded at a spectral resolution of 0.5 cm^{-1}, is a mean spectrum averaged over latitudes 10°S - 10°N and over emission angle 20° - 30°. (A) CIRS radiance. (B) Corresponding brightness temperature.

Figure 2. Coverage of wavenumber-integrated CIRS radiance in the plane of latitude and emission angle. (A) FP1. (B) FP3. (C) FP4. The limited coverage of FP1 is due to its large field of view with respect to FP3 and FP4.

Figure 3. VIMS maps at 5 μm. (A) Map with unit of I/F. (B) Map with unit of radiance. (C) Night-side map with unit of radiance. The emission angle increases from ~ 0° at the center of disk to ~ 90° at the limb of disk. The spatial resolution of the VIMS maps is ~ 3° in both latitude and longitude.

Figure 4. Least-squares fitting of the CIRS observations by the focal planes FP3 and FP4 at different latitudes. The red dots are observations, and the blue lines are fitted lines. Panels (A), (B), (C), (D), and (E) are fits for the FP3 observations at 60°N, 30°N, 0°, 30°S, and 60°S, respectively. Panels (F), (G), (H), (I), and (J) are same as (A), (B), (C), (D), and (E) except for the FP4 observations.

Figure 5. Filling the FP3 observational gaps (panel B of Fig. 2) with the interpolation/extrapolation by the least-squares fit. (A) Raw FP3 radiance and the fitted data. (B) Ratio of fitted residual to the raw observational data.

Figure 6. Same as Fig. 5 except for the FP4 radiance.

Figure 7. Scatter plots of the FP1 radiances and the FP3 radiances. Only these latitude bins with the number of the simultaneous FP1 and FP3 observations more than 10 are shown. Panels (A), (B), (C), (D), (E), (F), (G), (H), and (I) are for the observations at 10°N, 9°N, 8°N, 7°N, 6°N, 3°N, 1°N, 4°S, and 5°S, respectively.

Figure 8. Ratio of wavenumber-integrated radiance between FP1 and FP3 (FP1/FP3). The plot is for the overlap areas observed by both FP1 and FP3.

Figure 9. Zonal mean and standard deviation of the radiance ratio FP1/FP3. The zonal mean and standard deviation are along the direction of emission angle, which is based on the plane of latitude and emission angle shown in Fig. 7. (A) Zonal mean of the ratio; (B) Standard deviation (std) of the ratio; and (C) Ratio of standard deviation to zonal mean.

Figure 10. Zonal mean of FP3 radiance and the comparison between the observed ratio FP1/FP3 and the regressed ratio FP1/FP3. (A) Zonal mean of the FP3 radiance. The zonal mean of the

FP3 radiance is along the direction of emission angle, which is based on the panel A of Fig. 5. (B) Comparison of the ratio FP1/FP3 between the regression and the observation.

Figure 11. Filling the FP1 observational gaps by the linear regression of the FP3 radiance. (A) Raw FP1 radiance and regressed FP1 data. The regressed FP1 data are based on the FP3 radiance (panel A of Fig. 5) and the regressed ratio FP1/FP3 (panel B of Fig. 9). (B) Ratio of the regression residual to the raw observational data.

Figure 12. Meridional profile of the emitted power in the wavenumber range of Cassini/CIRS (10-1430 cm^{-1}). The solid line is the profile of emitted power. The stippling represents the uncertainty of emitted power, which includes different uncertainty sources from the calibration, the filling of the observational gaps, and the variation of Jupiter's radiance along the longitude.

Figure 13. Comparison of the global-average 5-μm spectra between Voyager/IRIS and Cassini/VIMS. The spectral resolutions are ~ 0.005μm and ~ 0.017μm for Voyager/IRIS and Cassini/VIMS, respectively.

Figure 14. Meridional profile of the emitted power from the 5-μm thermal band (1800-2250 cm^{-1} ~ 4.4-5.6 μm). The solid line is the profile of emitted power, and the stippling represents the uncertainty of measurements.

Figure 15. Meridional profile of Jupiter's emitted power and effective temperature. The solid line is the profile of emitted power and effective temperature, and the stippling represents the uncertainty of measurements.

Figure 16. Comparison between the effective temperature and the atmospheric temperature in the Cassini epoch. The red line is Jupiter's effective temperature during the period of October, 2000 – March, 2001. The blue lines are the atmospheric temperatures of Jupiter in the roughly same period (Simon-Miller et al., 2006).

Figure 17. Comparison of meridional profile of the emitted power and effective temperature between the Voyager epoch and the Cassini epoch. The Voyager profile is mainly based on the Voyager observations in 1979 (Pirraglia, 1984). The Voyager profile in the high latitudes comes from the Pioneer observations (Ingersoll et al., 1975, Ingersoll, 1990). The uncertainty of the Voyager profile comes from the estimates by Pirraglia (1984). The Cassini profile comes from Fig. 14.

Figure 18. Comparison between the effective temperature and the atmospheric temperature in the Voyager epoch. The profile of Jupiter's effective temperature (i.e., red line) comes from Fig. 16. The profiles of Jupiter's atmospheric temperature (i.e., blue lines) comes from a previous study by Simon-Miller et al. (2006).

Figure 19. Temporal variation of the atmospheric temperature from the Voyager epoch to the Cassini epoch as a function of atmospheric pressure and latitude. There is no available

Cassini/CIRS retrieved temperature for the atmospheric layers deeper than 430 mbar due to the limitation of the content information in Jupiter's spectra.

Figure 20. Comparion of solar flux at the top of Jupiter's atmosphere between the Voyager epoch and the Cassini epoch. The meridional profile of solar flux is determined by the four factors (i.e., obliquity, eccentricity, incidence angle, and incidence time). The effects due to rings' shadowing and Jupiter's precession are too small to be considered in the computation.

Table 1 Hemispheric average of the emitted power and effective temperature of Jupiter during the Cassini epoch (i.e., 2000-01).

	NH average	SH average
Emitted power (W/m^2)	14.30	13.89
Uncertainty (W/m^2)	± 0.03	± 0.02
Effective temperature (K)	126.03	125.11
Uncertainty (K)	±0.07	±0.05

Table 2 Global-average values of emitted power and effective temperature by Pioneer, Voyager, and Cassini.

	Pioneer 10/11	Voyager 1	Cassini
Time	December, 1973 and December, 1974	March, 1979	October, 2000 to March, 2001
Solar longitude	16.8°	169.5°	110.5°
Subsolar latitude	0.6°N	0.5°N	2.9°N
Emitted power (W/m^2)	13.8	13.59	14.10
Uncertainty (W/m^2)	± 1.4	± 0.14	± 0.02
Effective temperature (K)	125	124.4	125.57
Uncertainty (K)	±3	±0.3	±0.05

Note: The global values of Pioneer come from the study by Ingersoll et al. (1975). The global values of Voyager 1 come from the study by Hanel et al. (1981).

Figure 1

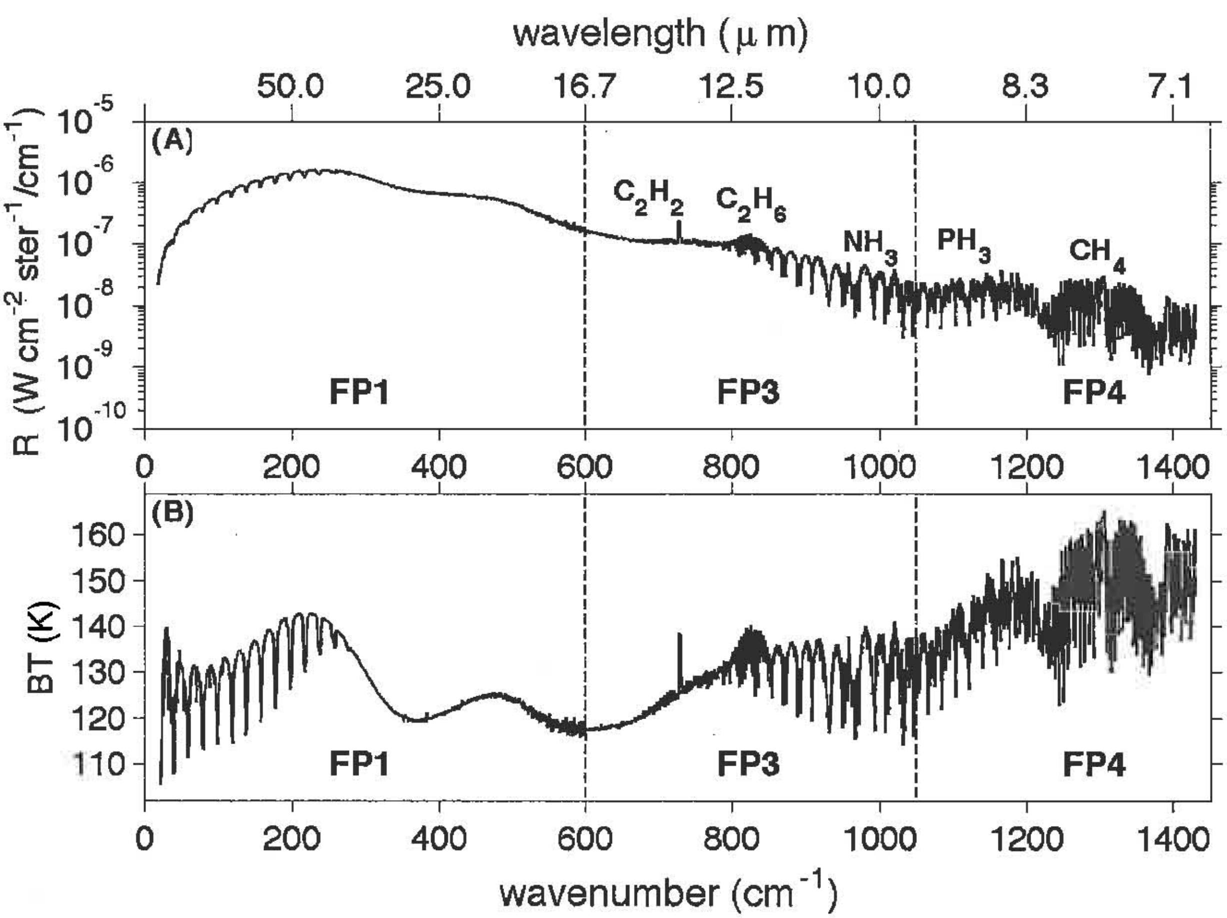

wavelength (μ m)
50.0
25.0
16.7
12.5
10.0
8.3
7.1
R (W cm^{-2} ster^{-1}/cm^{-1})
10^{-5}
10^{-6}
10^{-7}
10^{-8}
10^{-9}
10^{-10}
(A)
C_2H_2
C_2H_6
NH_3
PH_3
CH_4
FP1
FP3
FP4
(B)
BT (K)
160
150
140
130
120
110
0
200
400
600
800
1000
1200
1400
wavenumber (cm^{-1})

Figure 2

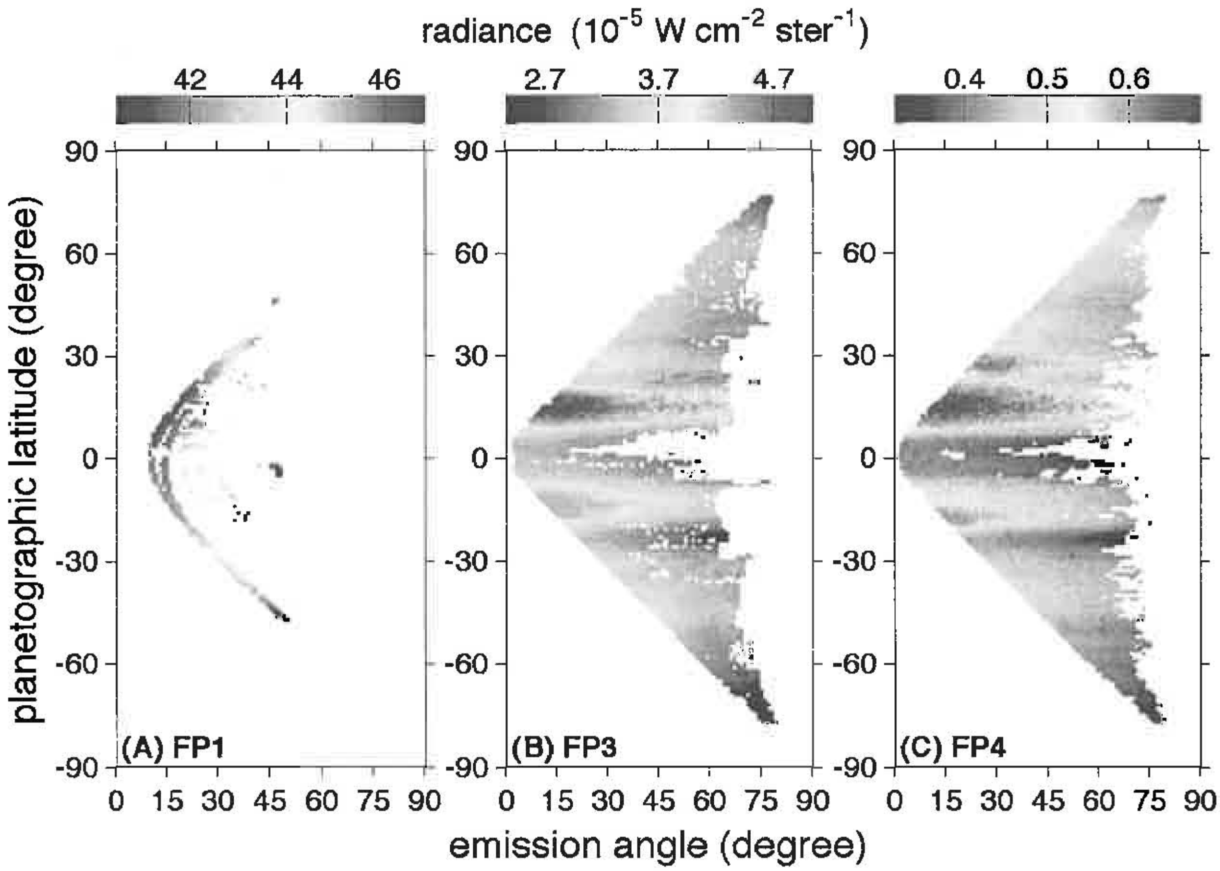
radiance (10^-5 W cm^-2 ster^-1)
42 44 46
2.7 3.7 4.7
0.4 0.5 0.6
planetographic latitude (degree)
90 60 30 0 -30 -60 -90
(A) FP1
(B) FP3
(C) FP4
0 15 30 45 60 75 90
emission angle (degree)

Figure 3

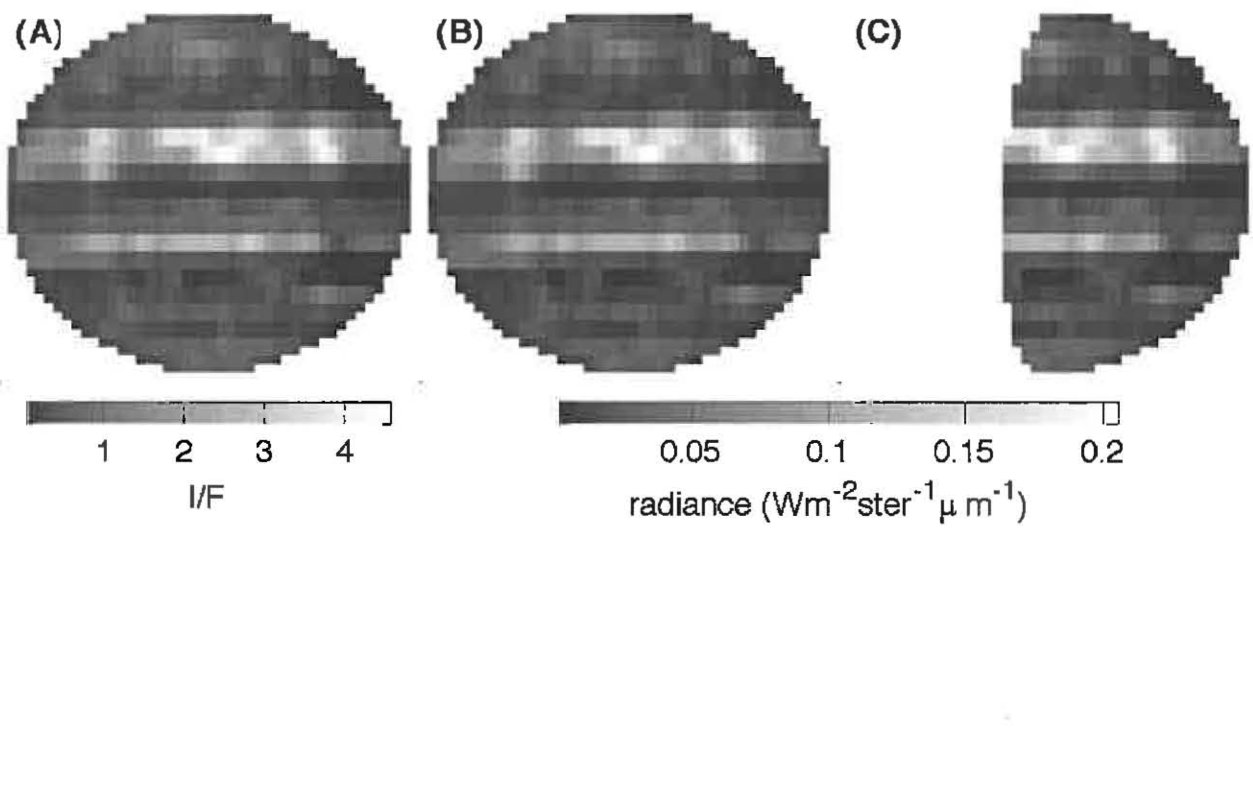

Figure 4

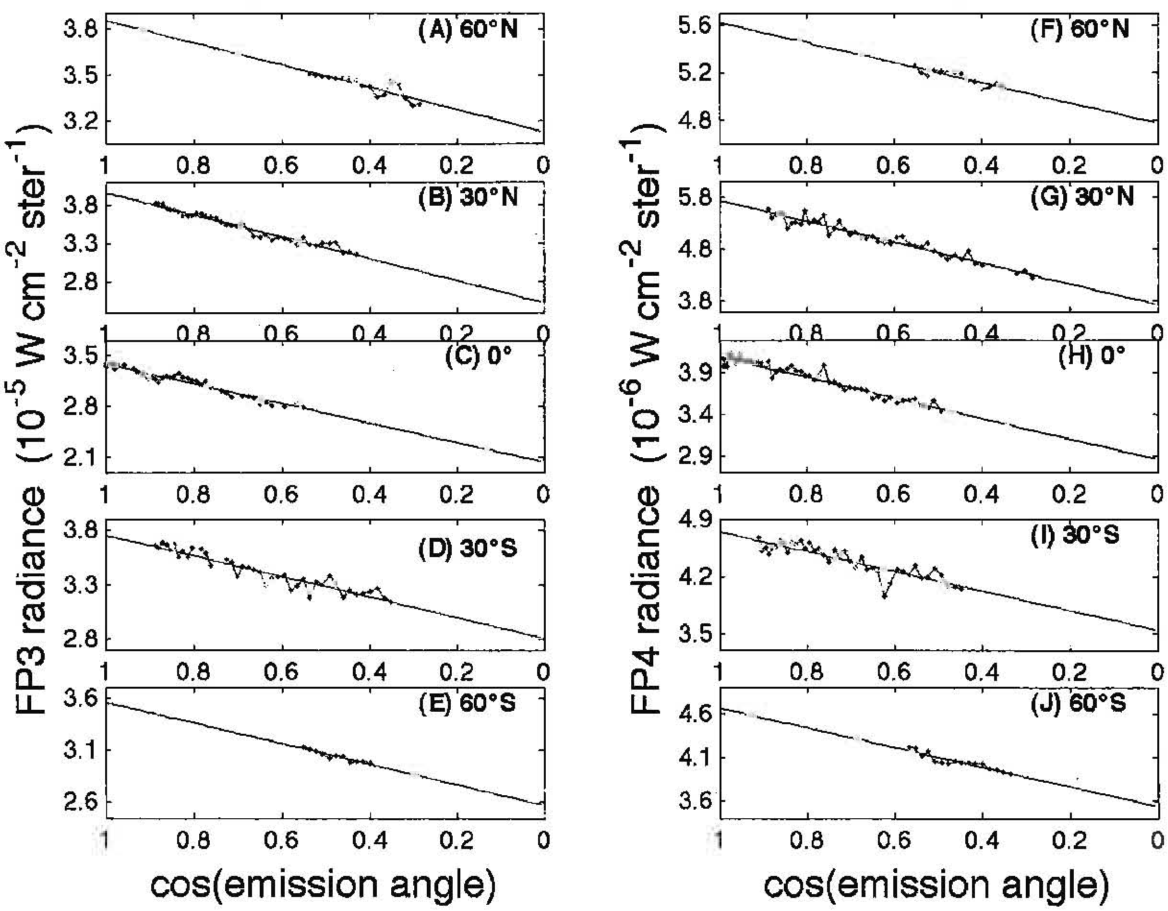
(A) 60°N
(B) 30°N
(C) 0°
(D) 30°S
(E) 60°S
(F) 60°N
(G) 30°N
(H) 0°
(I) 30°S
(J) 60°S
FP3 radiance (10^{-5} W cm^{-2} ster^{-1})
FP4 radiance (10^{-6} W cm^{-2} ster^{-1})
cos(emission angle)
cos(emission angle)

Figure 5

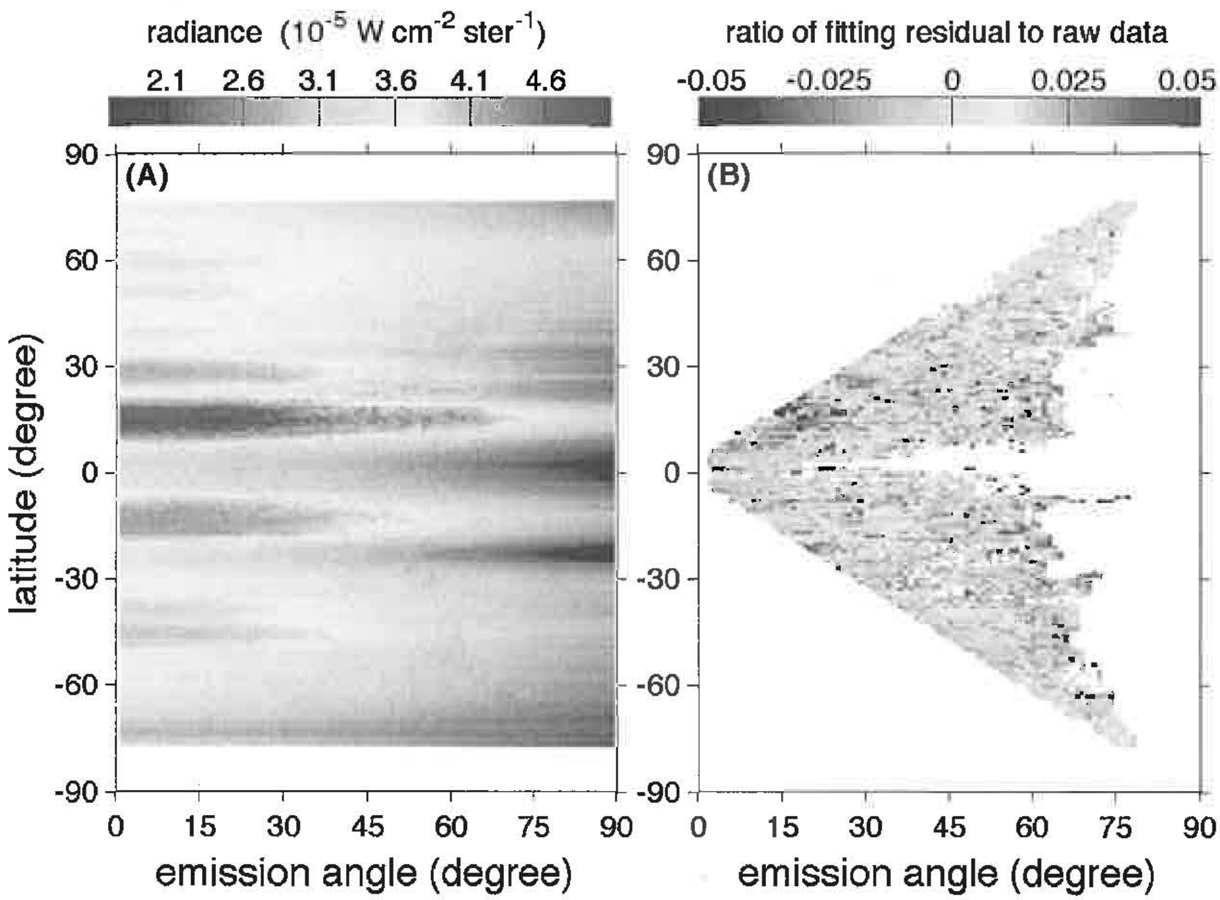
radiance (10^{-5} W cm^{-2} ster^{-1})
2.1 2.6 3.1 3.6 4.1 4.6
ratio of fitting residual to raw data
-0.05 -0.025 0 0.025 0.05
(A)
(B)
latitude (degree)
90 60 30 0 -30 -60 -90
0 15 30 45 60 75 90
emission angle (degree)
emission angle (degree)

Figure 6

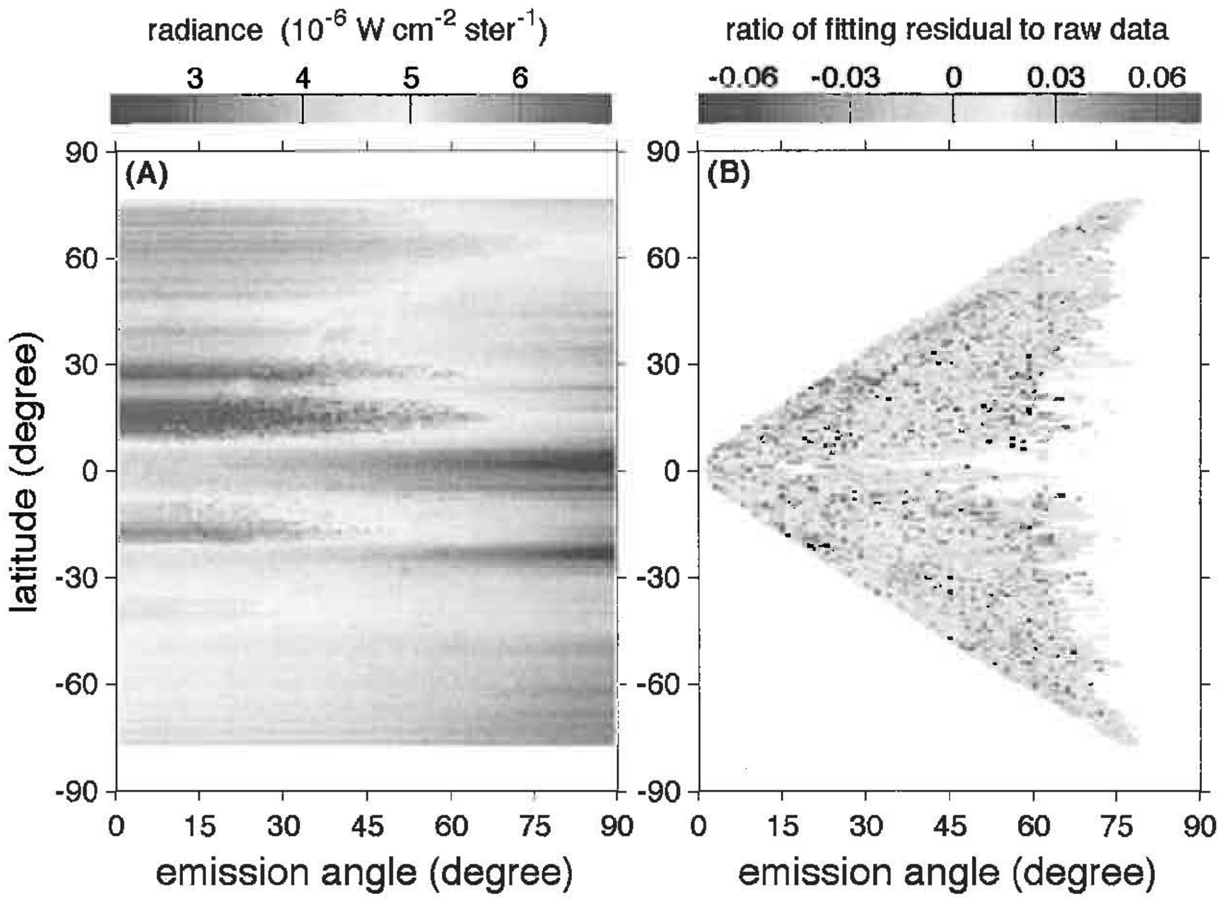
radiance (10^-6 W cm^-2 ster^-1)
3
4
5
6
ratio of fitting residual to raw data
-0.06
-0.03
0
0.03
0.06
(A)
(B)
latitude (degree)
90
60
30
0
-30
-60
-90
0
15
30
45
60
75
90
emission angle (degree)
emission angle (degree)

Figure 7

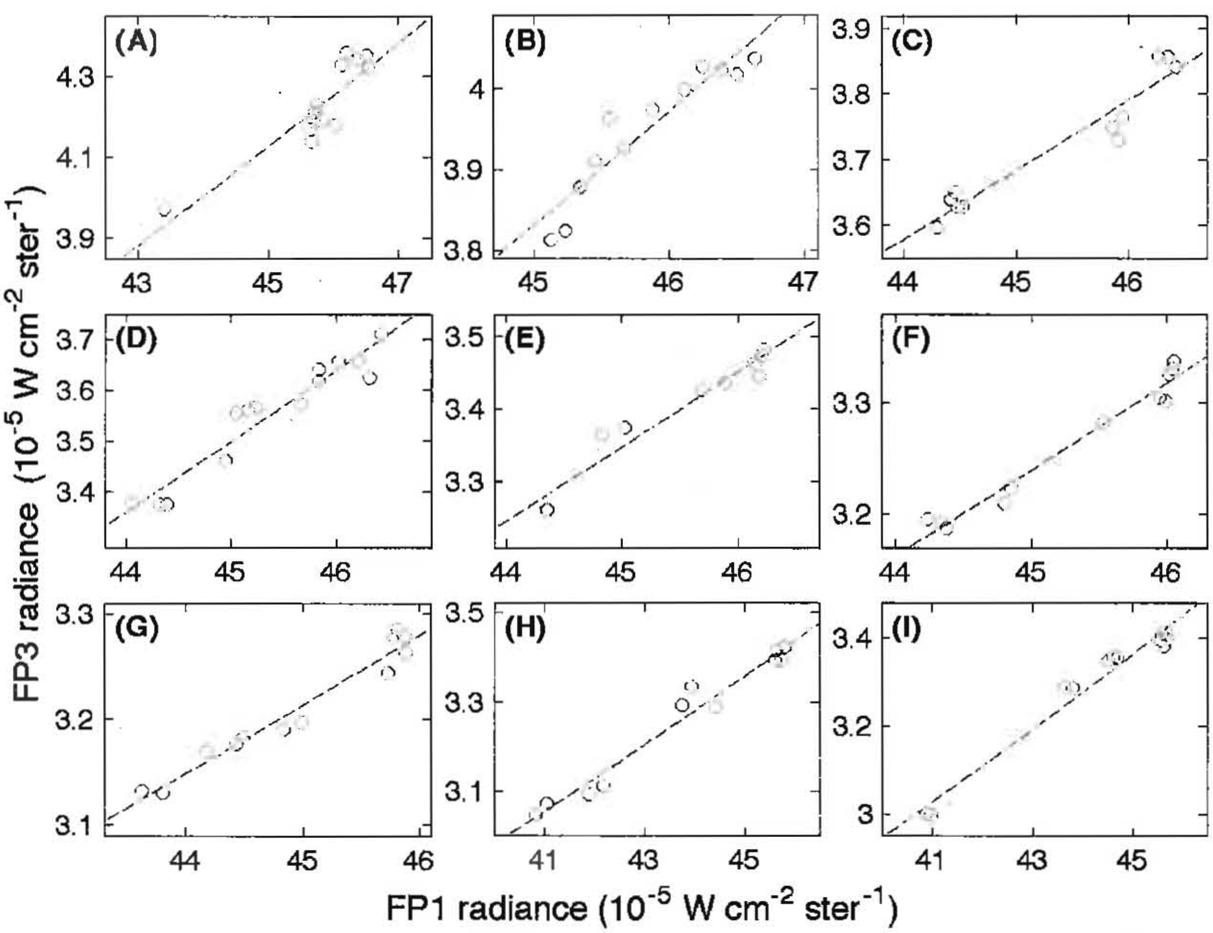

(A)
(B)
(C)
(D)
(E)
(F)
(G)
(H)
(I)
FP3 radiance (10^-5 W cm^-2 ster^-1)
FP1 radiance (10^-5 W cm^-2 ster^-1)

Figure 8

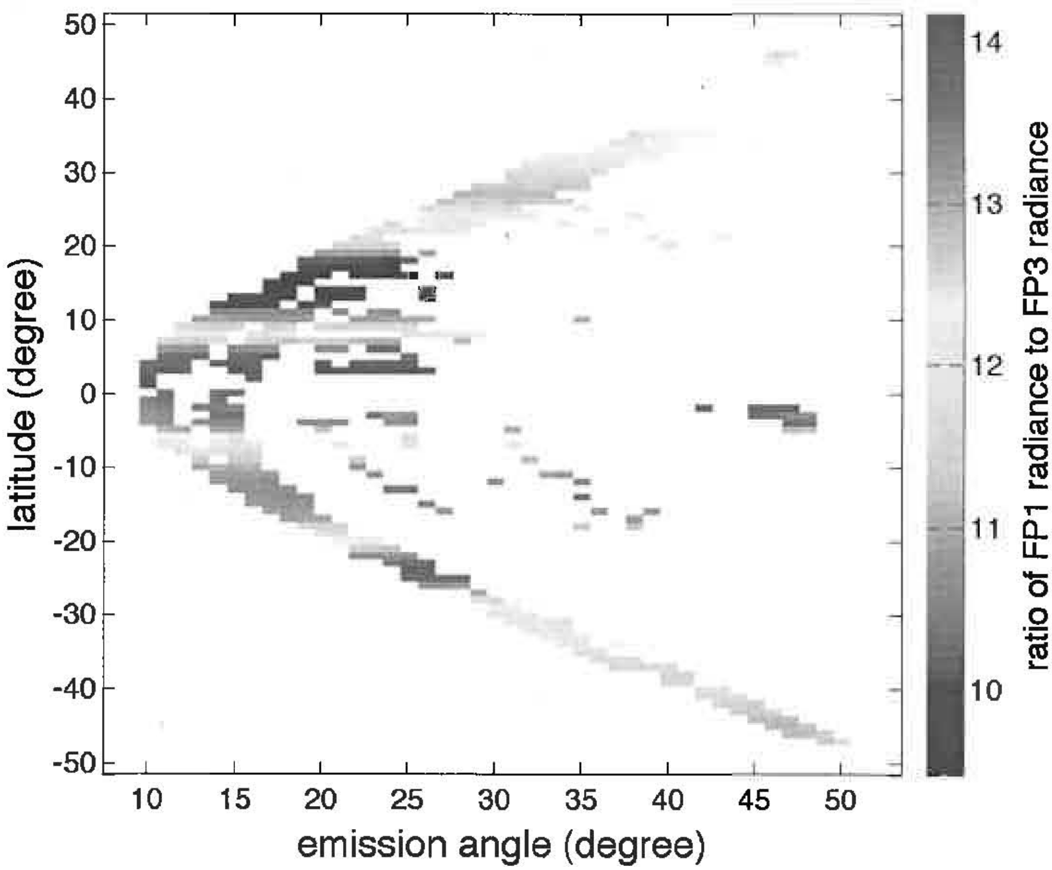
latitude (degree)
emission angle (degree)
ratio of FP1 radiance to FP3 radiance
50
40
30
20
10
0
-10
-20
-30
-40
-50
10
15
20
25
30
35
40
45
50
14
13
12
11
10

Figure 9

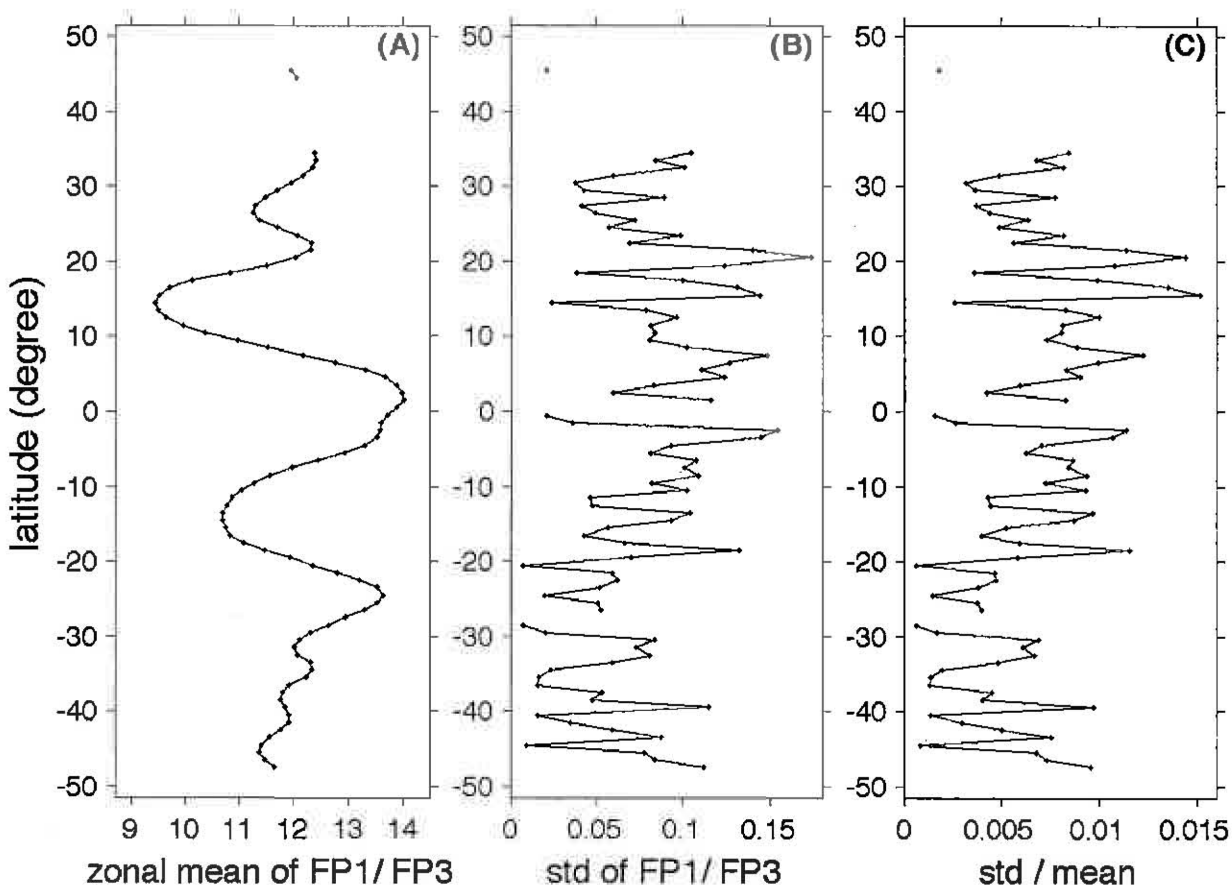
(A)
(B)
(C)
latitude (degree)
50
40
30
20
10
0
-10
-20
-30
-40
-50
9 10 11 12 13 14
zonal mean of FP1/ FP3
0 0.05 0.1 0.15
std of FP1/ FP3
0 0.005 0.01 0.015
std / mean

Figure 10

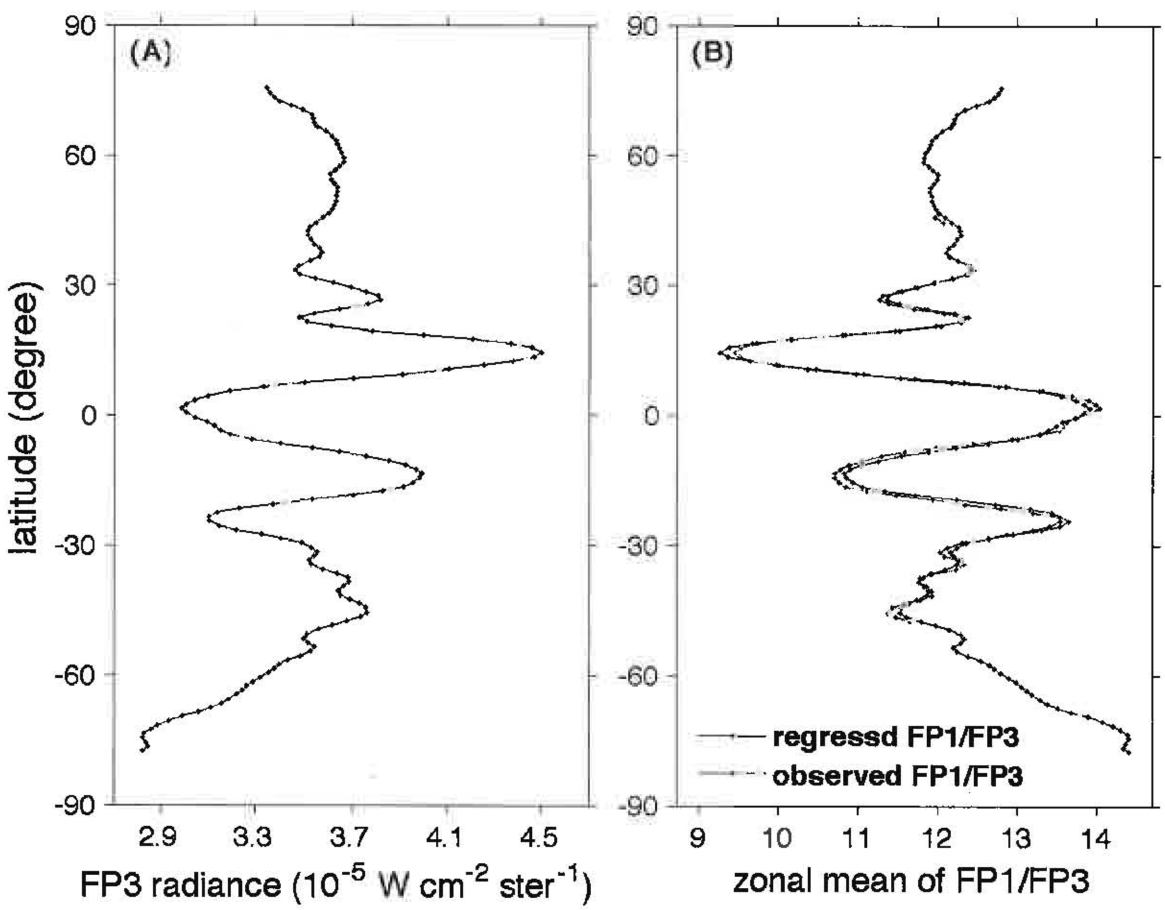
(A)
(B)
latitude (degree)
90
60
30
0
-30
-60
-90
2.9
3.3
3.7
4.1
4.5
FP3 radiance (10^{-5} W cm^{-2} $ster^{-1}$)
9
10
11
12
13
14
zonal mean of FP1/FP3
regressd FP1/FP3
observed FP1/FP3

Figure 11

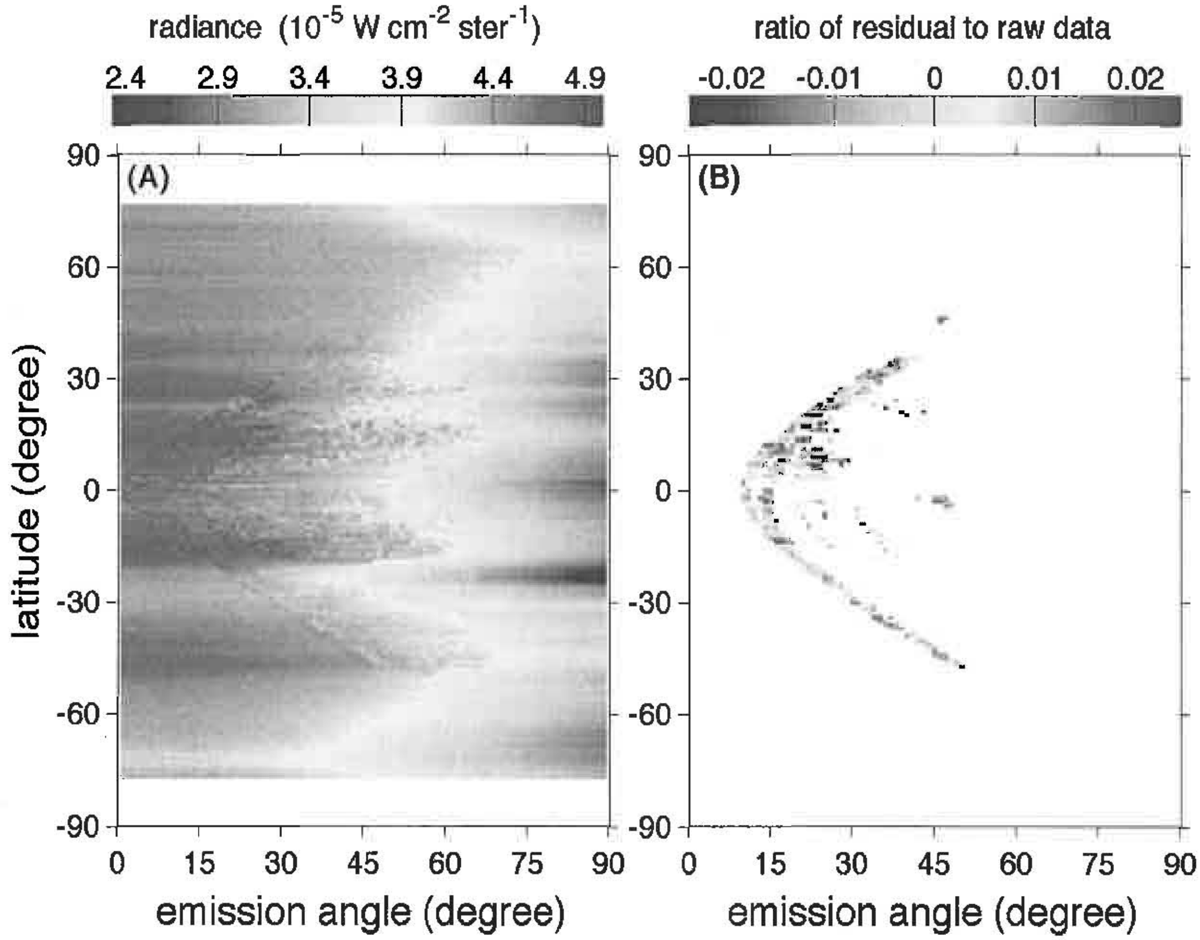
radiance (10^{-5} W cm^{-2} ster^{-1})
2.4 2.9 3.4 3.9 4.4 4.9
ratio of residual to raw data
-0.02 -0.01 0 0.01 0.02
(A)
(B)
latitude (degree)
90 60 30 0 -30 -60 -90
0 15 30 45 60 75 90
emission angle (degree)

Figure 12

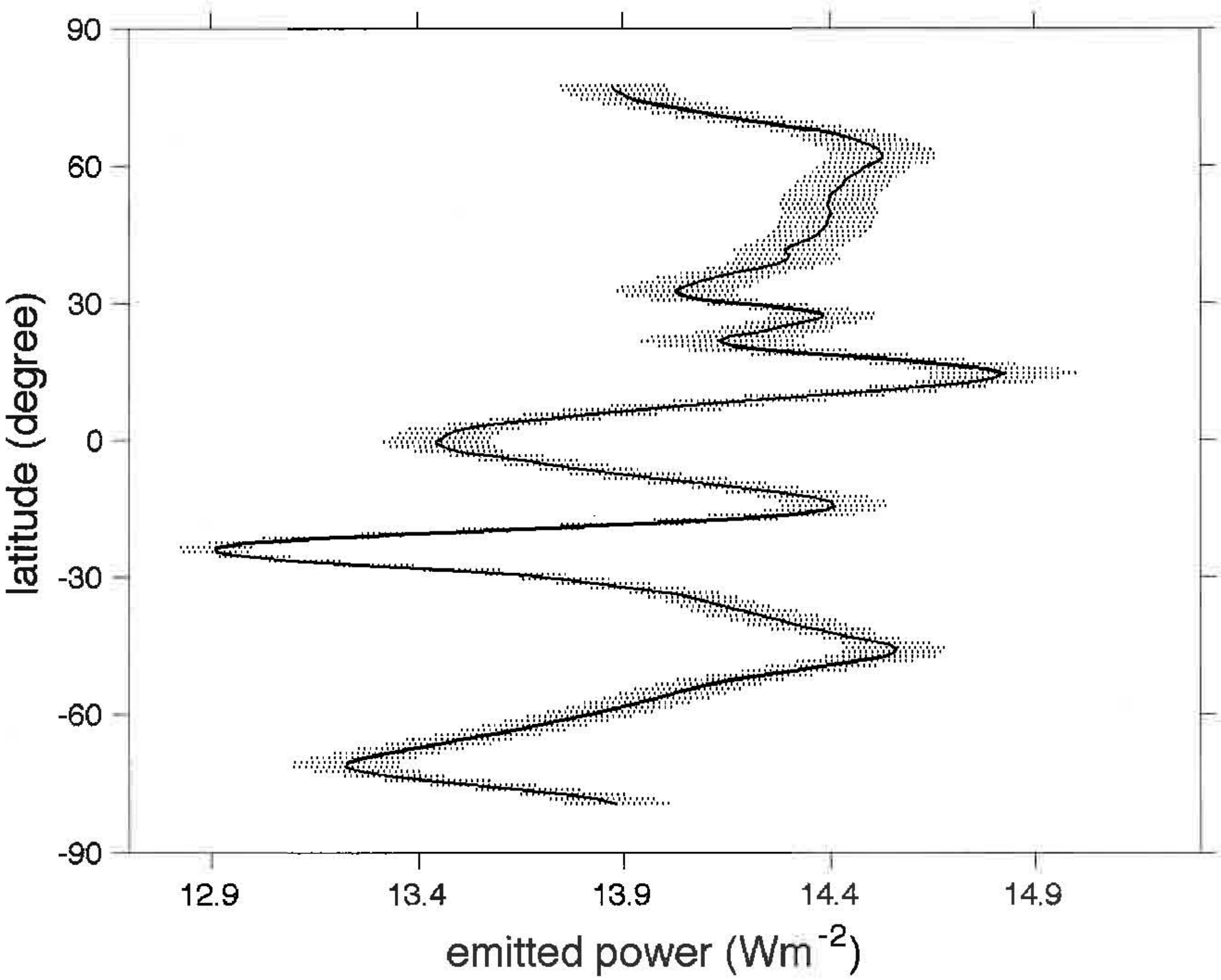

90
60
30
0
-30
-60
-90
latitude (degree)
12.9
13.4
13.9
14.4
14.9
emitted power (Wm^-2)

Figure 13

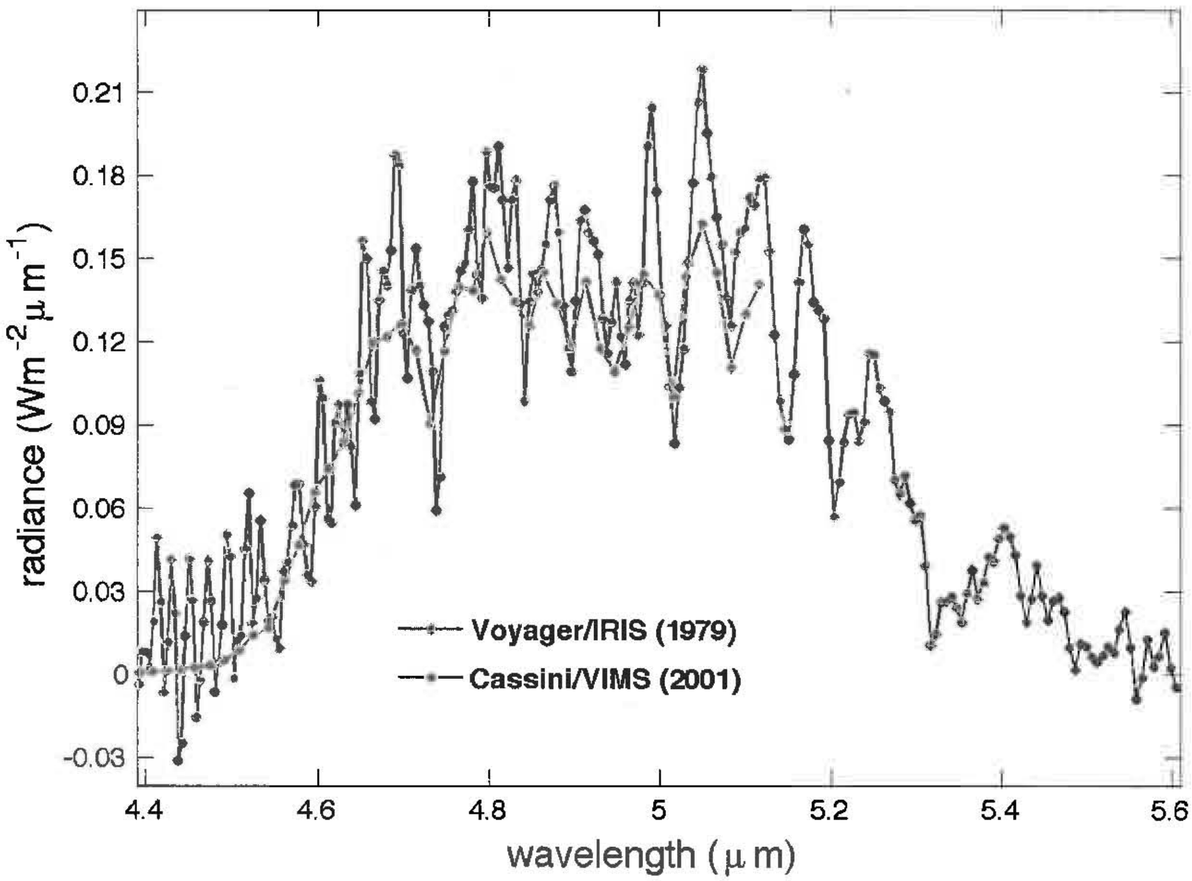

Voyager/IRIS (1979)
Cassini/VIMS (2001)
radiance (Wm $^{-2}$ μ m $^{-1}$)
wavelength (μ m)
0.21
0.18
0.15
0.12
0.09
0.06
0.03
0
-0.03
4.4
4.6
4.8
5
5.2
5.4
5.6

Figure 14

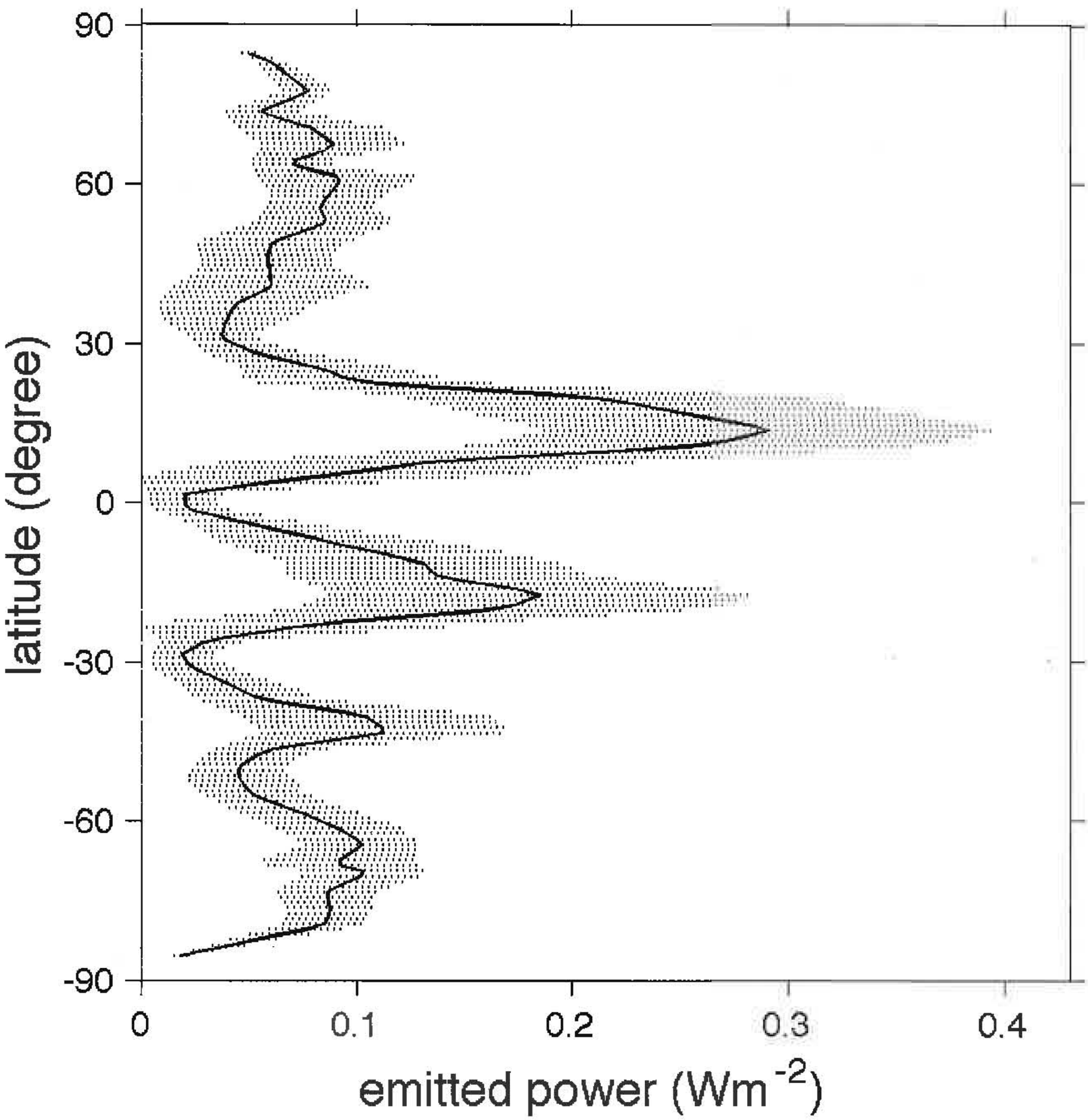
90
60
30
0
-30
-60
-90
latitude (degree)
0
0.1
0.2
0.3
0.4
emitted power (Wm -2)

Figure 15

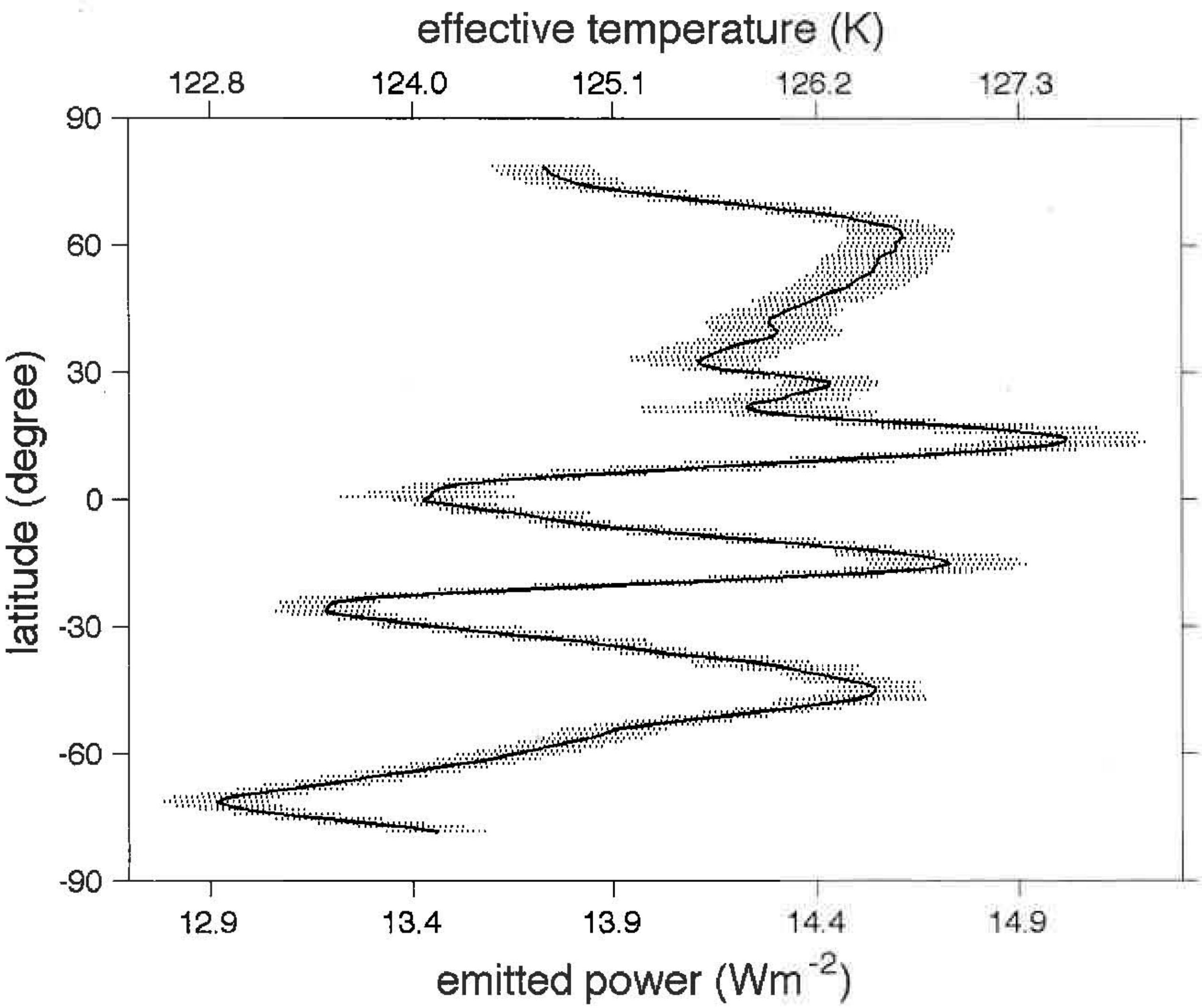
effective temperature (K)
122.8
124.0
125.1
126.2
127.3
latitude (degree)
90
60
30
0
-30
-60
-90
12.9
13.4
13.9
14.4
14.9
emitted power (Wm -2)

Figure 16

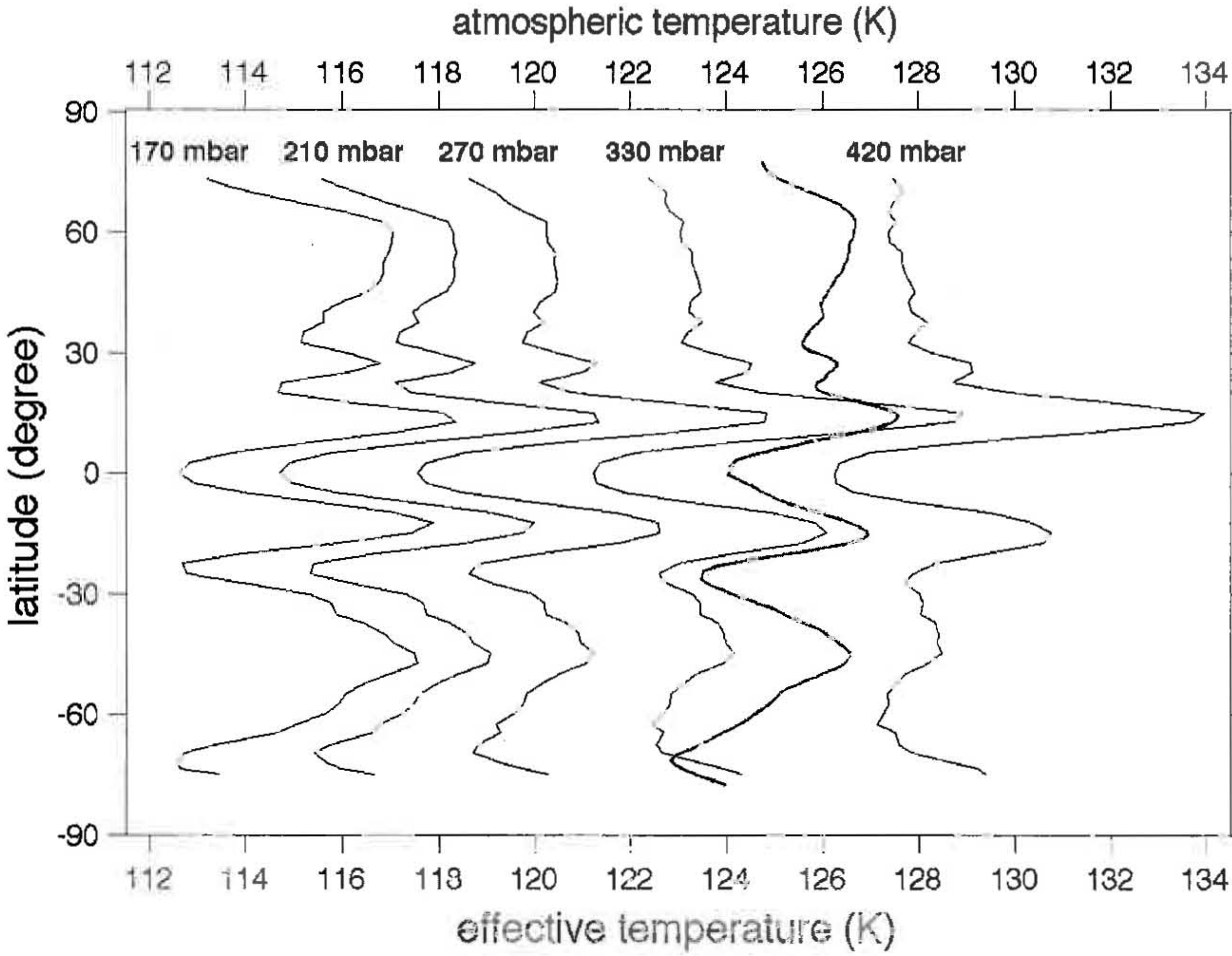

Figure 17

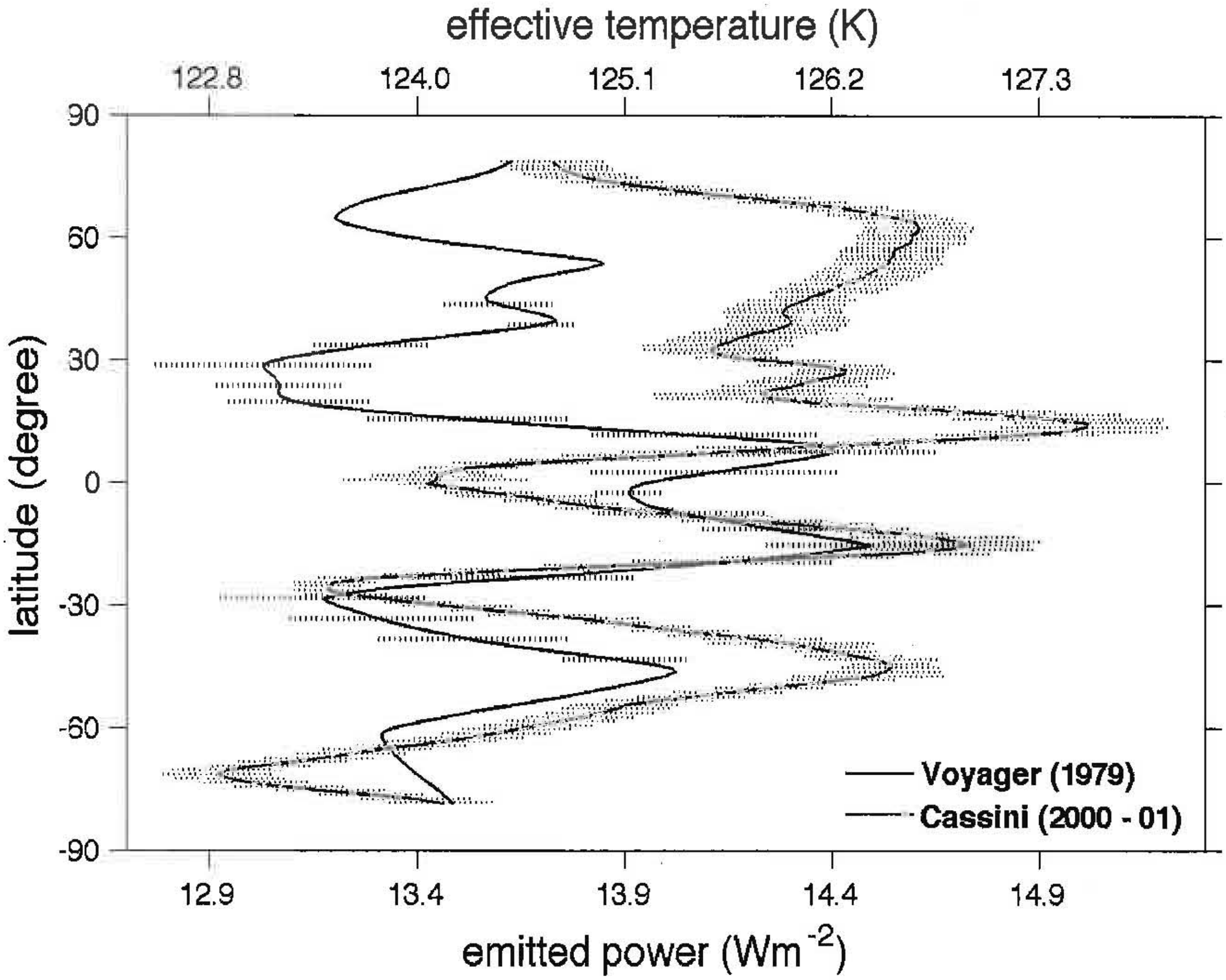
effective temperature (K)
122.8
124.0
125.1
126.2
127.3
90
60
30
0
-30
-60
-90
latitude (degree)
Voyager (1979)
Cassini (2000 - 01)
12.9
13.4
13.9
14.4
14.9
emitted power (Wm-2)

Figure 18

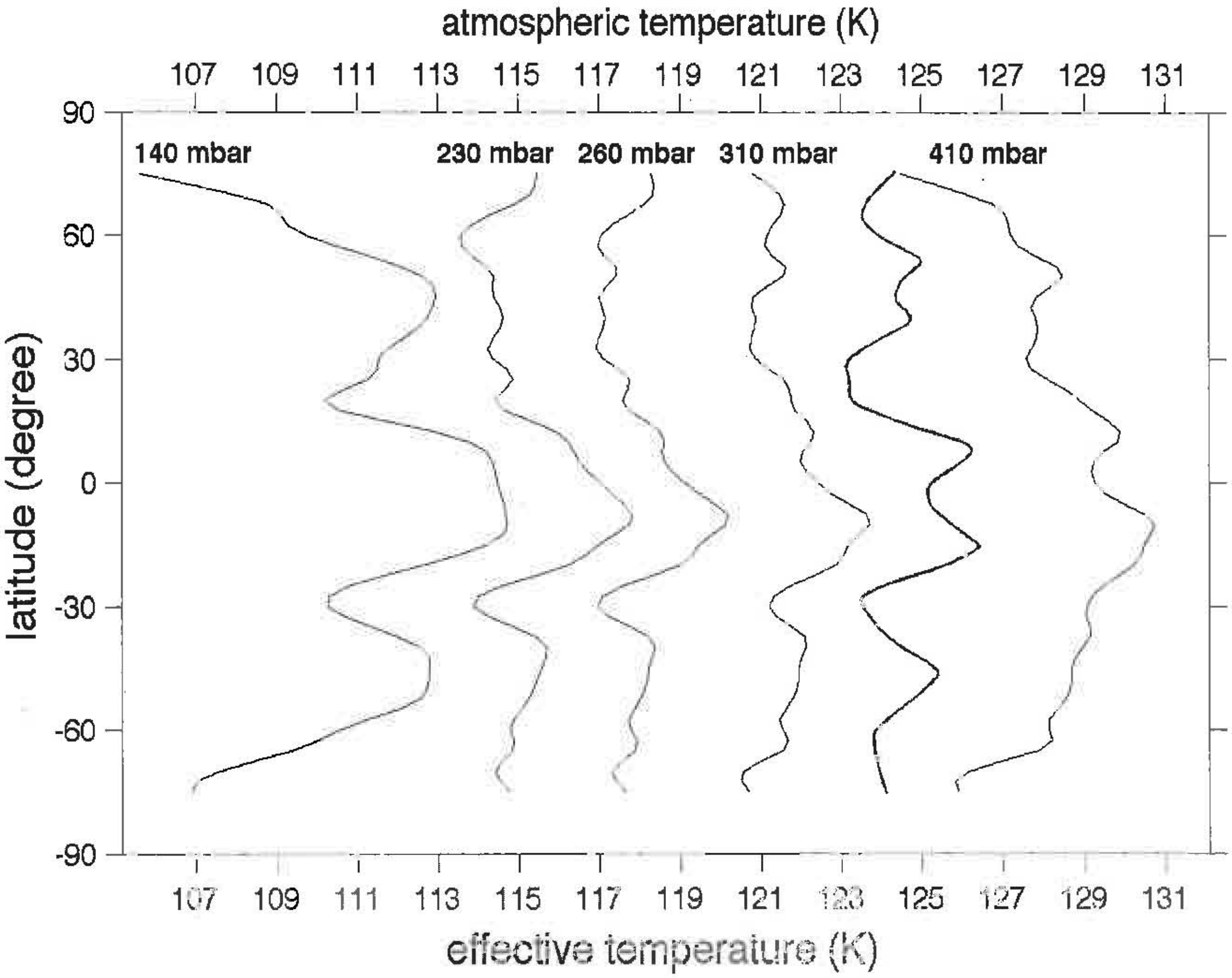
atmospheric temperature (K)
107 109 111 113 115 117 119 121 123 125 127 129 131
140 mbar
230 mbar
260 mbar
310 mbar
410 mbar
latitude (degree)
90 60 30 0 -30 -60 -90
107 109 111 113 115 117 119 121 123 125 127 129 131
effective temperature (K)

Figure 19

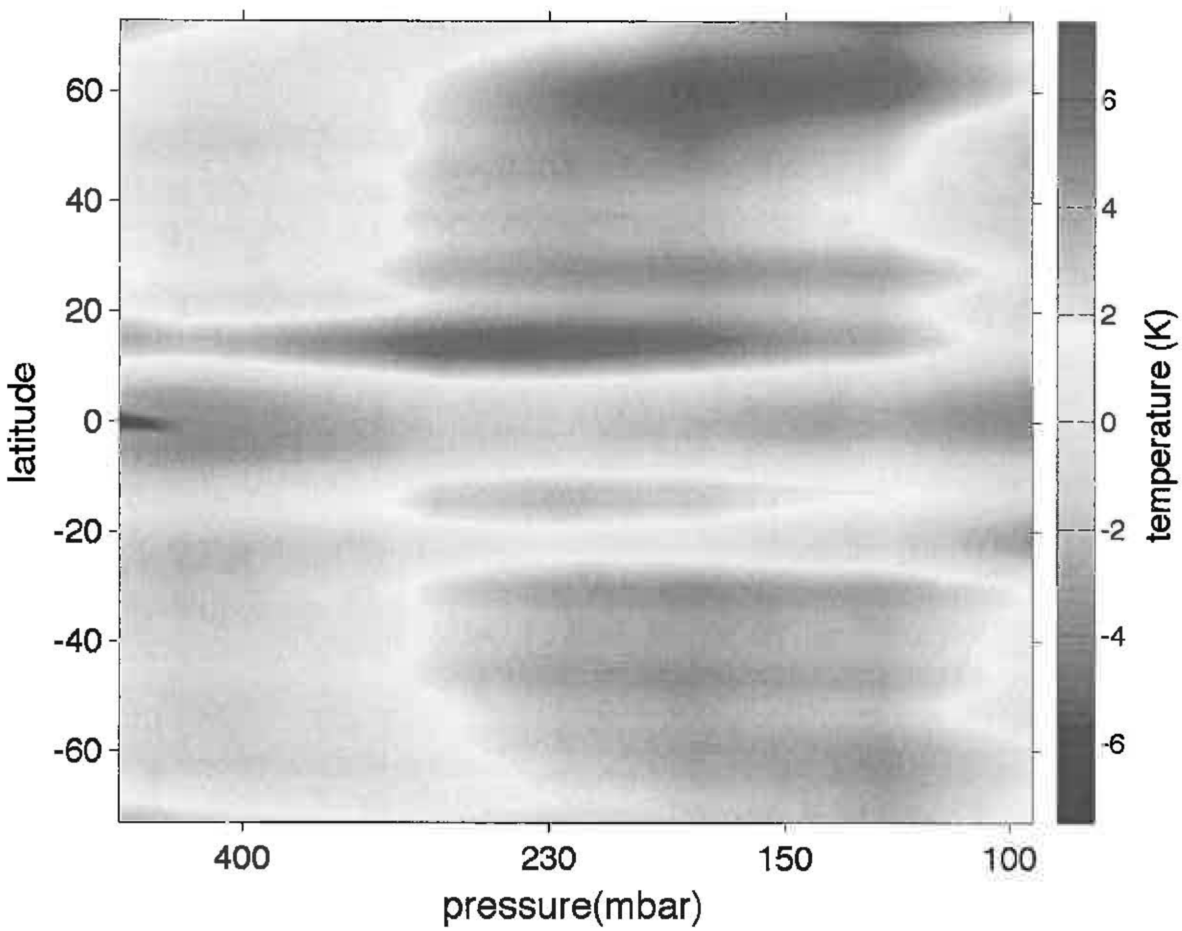
60
40
20
0
-20
-40
-60
latitude
400
230
150
100
pressure(mbar)
6
4
2
0
-2
-4
-6
temperature (K)

Figure 20

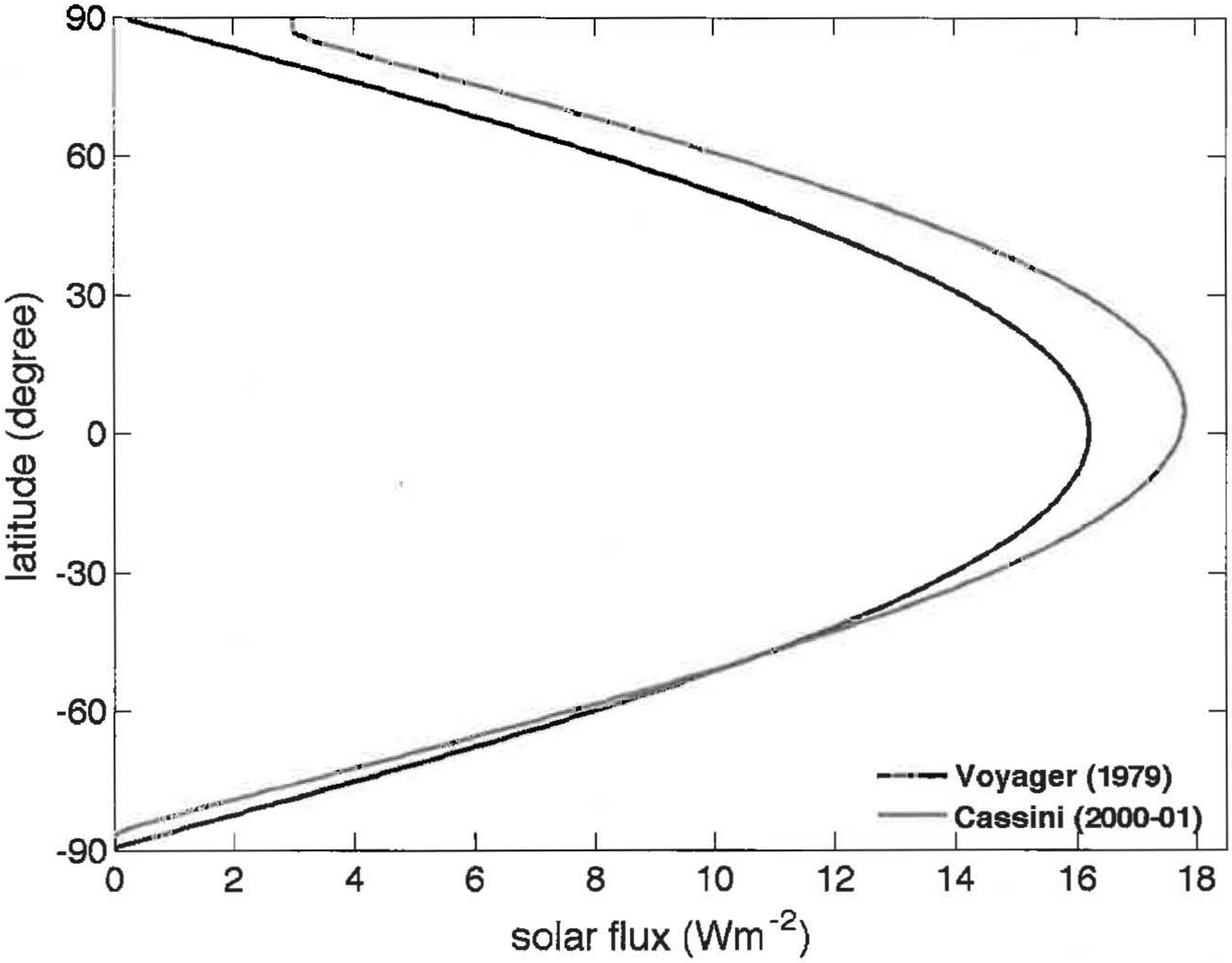
latitude (degree)
90
60
30
0
-30
-60
-90
0
2
4
6
8
10
12
14
16
18
solar flux (Wm^{-2})
Voyager (1979)
Cassini (2000-01)